RUPRECHT-KARLS-UNIVERSITÄT HEIDELBERG

Michael Neumann

A Novel Technique to Measure Thermal Conductivity of Amorphous Dielectrics at Very Low Temperature

Diplomarbeit

HD-KIP-03-12

KIRCHHOFF-INSTITUT FÜR PHYSIK

Faculty of Physics and Astronomy

University of Heidelberg

Diploma thesis

in Physics

submitted by

Michael Neumann

born in Heidelberg

2003

A Novel Technique to Measure Thermal Conductivity of Amorphous Dielectrics at Very Low Temperature

This diploma thesis has been carried out by Michael Neumann

at the Kirchhoff Institute of Physics

under the supervision of

Priv.-Doz. Dr. Christian Enss

Eine neuartige Meßtechnik zur Bestimmung der Wärmeleitfähigkeit amorpher Dielektrika bei sehr tiefen Temperaturen

Die hier vorgestellte Meßtechnik ist zu Wärmeleitfähigkeitsmessungen an dielektrischen Substanzen im Temperaturbereich hinunter bis zu mindestens 5 mK geeignet. Sie vereint eine paramagnetische SQUID-Thermometrietechnik mit einer optischen Heizmethode, und erreicht auf diesem Wege einen äußerst geringen parasitären Wärmeeintrag. Messungen wurden an Glasproben aus BK7 und Suprasil durchgeführt. Die vorgestellten Meßergebnisse besagen, daß die Wärmeleitfähigkeit dieser Proben bis 5 mK eine quadratische Temperaturabhängigkeit aufweist.

A Novel Technique to Measure Thermal Conductivity of Amorphous Dielectrics at Very Low Temperature

The technique presented here facilitates thermal conductivity measurements on dielectric samples down to at least 5 mK. It combines a paramagnetic SQUID thermometry technique with an optical heating method, attaining an extremely low level of parasitic heat input. Measurements were performed on BK7 and Suprasil glass samples. Results are presented, which show that thermal conductivity of these samples scales quadratically in temperature down to 5 mK.

Table of Contents

1. Introduction

The low temperature behavior of disordered solids has been studied intensively since the early 1970s, when Zeller and Pohl pointed out that in measurements of the thermal properties below 10 K, glasses behave fundamentally different from crystalline dielectrics. Since then, a wealth of experiments has been performed to measure the acoustic, dielectric, mechanical, thermal and other properties of various amorphous substances over the entire accessible temperature range, during which a large number of low temperature "anomalies" were discovered. Meanwhile, an abundance of theoretical attempts to explain the properties of amorphous materials at low temperature have been put forward.

An essential insight from this research was that glassy substances exhibit a universality in their properties at low temperature. For example, measurements of the thermal properties below 10 K reveal a behavior that is both qualitatively and quantitatively very similar for different amorphous dielectrics despite very diverse chemical composition. This universality suggests that, unlike in crystalline materials, whose properties are explained theoretically mainly on the basis of their microscopic structure, in a description of amorphous materials, the exact nature of the "disorder" on a microscopic scale does not play a crucial role. This is reflected by the fact that the "Standard Tunneling Model", which is a purely phenomenological model, manages to describe many of the low temperature properties of amorphous solids successfully. It is this universal behavior that has prompted much of the interest received by the research in amorphous materials.

On the experimental side, one of the main difficulties in performing experiments on amorphous substances at very low temperature is the extremely low tolerance of the measurements to parasitic heat input. Towards lower temperatures, the poor thermal conductivity of glasses diminishes even more, and so does their heat capacity, which leads to a very high sensitivity to external disturbing influences. Due to this, measurements of the thermal conductivity have so far been confined to the temperature range above 10 mK.

In this thesis, after a brief review of the Standard Tunneling Model, a new technique will be described which facilitates thermal conductivity measurements on glass in the Millikelvin temperature range. We have performed such measurements down to temperatures as low as 5 mK, which is a factor of 2 less than the lowest temperature attained in previous experiments employing other techniques. Our results, obtained from BK7 and Suprasil glass samples, demonstrate that the thermal conductivity of these materials has an approximately quadratic temperature dependence down to 5 mK, i.e., $\kappa \propto T^2$, in accordance with the predictions of the Standard Tunneling Model.

2. Theoretical Introduction

2.1 Thermal Anomalies at Low Temperature

In crystalline dielectrics the thermal properties at temperatures below 1 K are well described by the Debye model (see for example Kittel (1996) or Hunklinger (2001)). In this model the solid is represented as an elastic continuum in which phonons propagate at constant velocities v_l and v_t. As the Debye model does not make any reference to the regular structure of the solid on a microscopic scale, there is no apparent reason why this model should not be applicable to amorphous substances as well. Especially at temperatures below 1 K, the wavelength of the dominant phonons is of the order of 1000 Å and thus significantly larger than the irregularities on an atomic scale.

However, in experiments at low temperature, both the specific heat and the thermal conductivity of amorphous materials turned out to differ markedly from the predictions of the Debye model, as it was first pointed out by Zeller and Pohl (1971). These deviations from the behavior of crystalline substances are labelled as "thermal anomalies".

2.1.1 Specific Heat

At low temperature, the specific heat of crystalline dielectrics is described by the Debye model, which correctly predicts a temperature dependency of T^3. This is in contrast to the behavior of amorphous materials, where below 1 K the specific heat depends approximately linearly on the

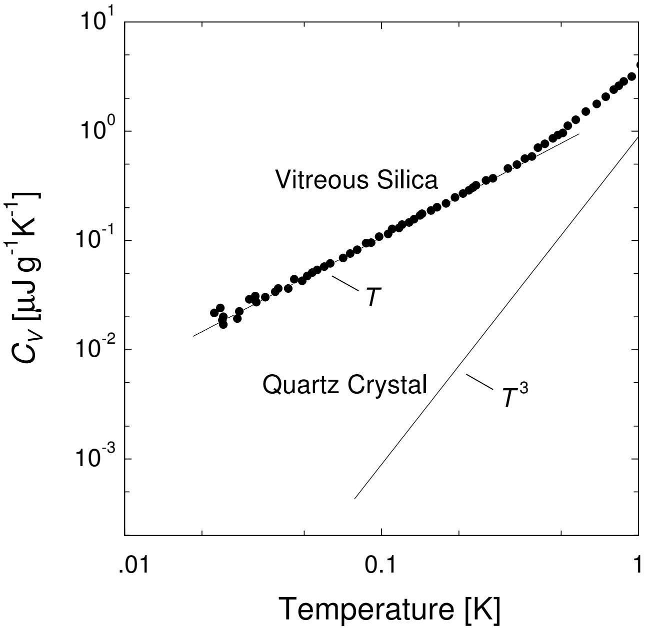

Fig. 2.1. Specific heat of crystalline SiO_2 and of vitreous silica below 1 K. Over all the temperature range the specific heat of the glassy modification is larger. (Lasjaunias et al. 1975)

temperature. Figure 2.1 uses SiO_2 as an example to display this qualitative difference, and it also demonstrates that the absolute value of the specific heat in the amorphous specimen is well above the one of its crystalline counterpart, with a difference of about three orders of magnitude at 25 mK. This suggests that the amorphous substance contains additional excitations on a low energy scale. Thus we can write the total specific heat of an amorphous substance as $C_{\text{tot}} = C_{\text{ph}} + C_{\text{extra}}$, where C_{ph} is the phonon contribution which is described by the Debye model, and C_{extra} is the term arising from the additional excitations. This "excess" specific heat of amorphous materials can be approximated as

$$C_{\text{extra}} = a_1 T^{1+\alpha} + a_3 T^3 , \tag{2.1}$$

i.e., there is a quasi-linear contribution, and an "excess" cubic contribution. The parameter α is a small number, usually between 0.1 and 0.3.

2.1.2 Thermal Conductivity

As shown in Fig. 2.2, crystalline and amorphous materials differ also in their thermal conductivity. According to Debye's theory, in crystalline dielectrics heat is conducted by phonons, which are scattered by each other through the anharmonic interactions, or by defects in the lattice, for example due to impurities. In analogy to the diffusion of gas molecules, the kinetic gas theory describes this process in terms of a so-called phonon gas, and obtains the thermal conductivity as

$$\kappa_{\text{ph}} = \frac{1}{3} C_{\text{ph}} \, v \, l , \tag{2.2}$$

where C_{ph} is the specific heat of the phonon gas, v the average sound velocity, and l the mean free path of the thermal phonons, which is determined by the scattering processes. At higher temperatures, scattering of phonons is mainly due to the interaction between the phonons, and the scattering rate decreases with temperature, resulting in a longer thermal mean free path.

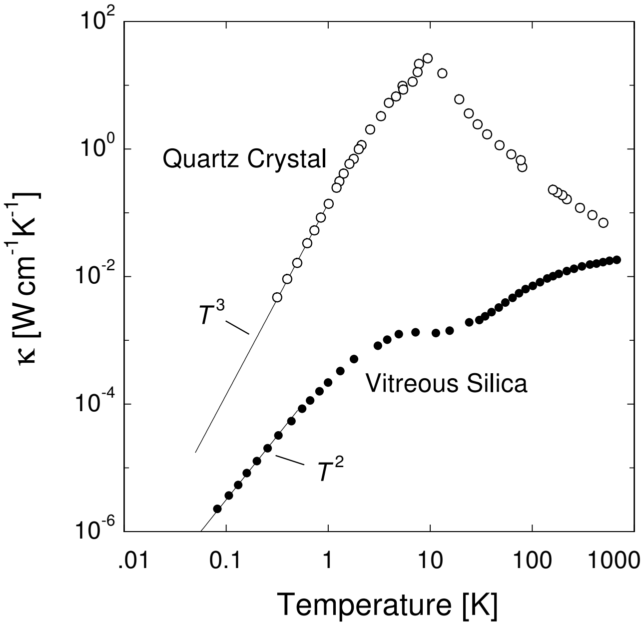

Fig. 2.2. Thermal conductivity of crystalline SiO_2 and of vitreous silica. (Zeller and Pohl 1971)

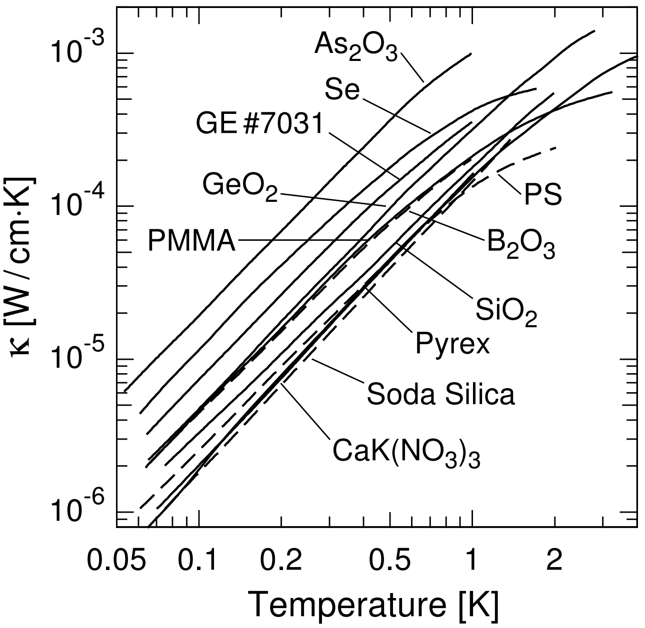

Fig. 2.3. Comparison of the thermal conductivities $\kappa(T)$ of different amorphous substances. The data on As_2O_3, Se, GE No. 7031 varnish, GeO2, polymethylmethacrylate (PMMA), polystyrene (PS), B_2O_3, SiO_2, soda silica $3\,SiO_2 \cdot Na_2O$, and $CaK(NO_3)_3$ are from Pohl, Love and Stephens (1974). The data on Pyrex are from Zeller and Pohl (1971).

Therefore, the thermal conductivity increases as T decreases, until it reaches a maximum at about 10 K. In the temperature region below the maximum, called the Casimir regime, the mean free path of the phonons becomes so large that it is essentially limited by scattering from defects at the specimen's surface, and l is constant. As the sound velocity v is also nearly constant in this temperature region the thermal conductivity is proportional to T^3.

Amorphous dielectrics exhibit a very different behavior. In the entire temperature range below room temperature their thermal conductivity is well below the one of crystalline substances. In the region around 10 K there exists a plateau in the thermal conductivity κ_{ph}, and below the plateau, κ_{ph} is roughly proportional to T^2. This reduction of the thermal conductivity indicates that glasses contain additional scattering centers not present in crystalline materials, which limit the phonons' mean free path.

Moreover, the similarities with regard to heat conduction properties of different kind of amorphous materials even go beyond sharing the same qualitative behavior. In their initial publication, Zeller and Pohl (1971) already stated that the absolute values of the thermal conductivities κ of various kinds of disordered materials are very close to each other, in their case to within a factor of 3. In Fig. 2.3, the thermal conductivities κ of a wide range of amorphous solids are compared for the low temperature range. Despite their greatly differing chemical compositions, the different substances have absolute values of κ that agree to within an order of magnitude over the entire temperature range.

Extending this idea of the universal low temperature properties of the glassy state, Freeman and Anderson (1986) showed that the thermal conductivities of many different amorphous substances have nearly the same magnitude when scaled with a single parameter. This parameter is called the "Debye temperature" Θ_{D}, in allusion to the concept describing the universal properties of crystalline dielectrics. In Table 2.1, some of the low temperature properties of several amorphous substances are listed for comparison.

	Vitreous Silica a-SiO$_2$	Borosilicate Glass BK7	Duran/ Pyrex	Se	PMMA
ρ [kg m^{-3}]	2200^a	2510^c	2230^f	4300^d	1200^a
v_l ($\overline{v}$) [m s^{-1}]	5800^b	6000^b	5647^g	(1300)^a	(1790)^a
v_t [m s^{-1}]	3800^b	3800^b	3457^g		
γ_l [eV]	0.32^b	0.34^b			
γ_t [eV]	0.65^c	0.65^c		0.14^c	0.27^c
$\overline{P}\,\gamma_\mathrm{t}^2$ [10^7 J m^{-3}]	0.92^c	1.19^c		0.10^c	0.11^c
Θ_D [K]	342^d			77^d	71^d
α [10^{-4} W cm^{-1}K^{-1}]	2.4^a	2.51^e	3.9^f	7.9^a	3.3^a
β	1.87^a	1.84^e	2.0^f	1.81^a	1.81^a

Table 2.1. Low temperature parameters of several amorphous solids. ρ denotes the density of the solid, v_l and v_t are the longitudinal and transversal sound velocities, respectively. (For Se and PMMA, only an average $\overline{v}$ of these were available.) The deformation potentials are γ_l and γ_t. The quantity $\overline{P}$ is the density of TLSs, as in Eq. (2.16), and Θ_D is the Debye temperature. The coefficients α and β are from the formula $\kappa = \alpha\,(T/1\ \mathrm{K})^{\beta}$. The cited references are:

[a] Stephens (1973)
[b] Hunklinger and Arnold (1976)
[c] Heuer (1998)
[d] Freeman and Anderson (1986)
[e] Rosenberg, Natelson and Osheroff (2000)
[f] Herrmannsdörfer and König (2000)
[g] Siebert (2001)

To date, no microscopic theory is available that would explain the anomalous low temperature thermal properties of amorphous materials. However, a phenomenological model, which is based on several simple assumptions, was developed by Anderson, Halperin, and Varma (1972) and, independently, by Phillips (1972). This model correctly predicts both the T^2 dependency of the thermal conductivity and the T proportionality of the specific heat. We will give a short introduction of this model in the following section.

2.2 Standard Tunneling Model

Soon after Zeller and Pohl had published their results on the low temperature anomalies of glass, a variety of different models were proposed in attempt to explain these discoveries. The most successful model among them was proposed by Anderson, Halperin, and Varma (1972) and Phillips (1972), and it was later named the Standard Tunneling Model.

2.2.1 Isolated Tunneling Defect: Double Well Potential

Unlike in perfect crystals where every atom has a well-defined single equilibrium position, in a glass there are instances where atoms, or groups of atoms, have more than one potential minimum

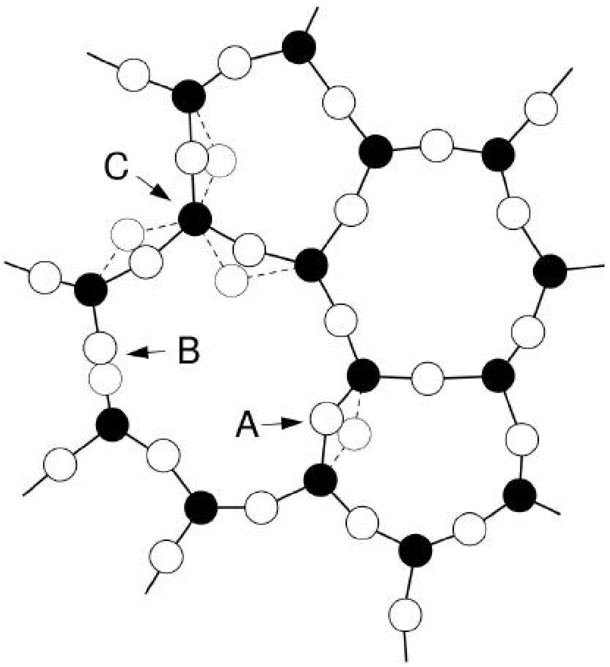

Fig. 2.4. Schematic of the structure of amorphous SiO_2. The full dots (●) represent the silicon atoms, while the oxygen atoms are drawn as empty circles (○). The configurations A, B and C are examples for systems where single atoms may assume two nearly equivalent equilibrium positions. (From Enss and Hunklinger (2000))

available, i.e., several minima are adjacent and on nearly equal energy levels. In Fig. 2.4 a two-dimensional schematic of the structure of amorphous SiO_2 is illustrated. The pattern of alternating silicon and oxygen atoms is like in crystalline quartz, but the number of atoms per ring and the bonding angles vary. Due to this irregular structure, some atoms may have access to more than one potential minimum. In the figure, the sites denoted as A, B and C are instances where an oxygen atom may assume one of two nearly equivalent potential minima, and indeed oscillates between the two. The two minima are separated by a potential barrier. If the oxygen atom cannot surmount this barrier via thermal activation, it may still move from one minimum to the other through quantum-mechanical tunneling. (It should be pointed out, however, that this representation is much simplified. In vitreous silica, as well as in other glasses, the entities moving between two potential minima seem to be more complex clusters, rather than single atoms.)

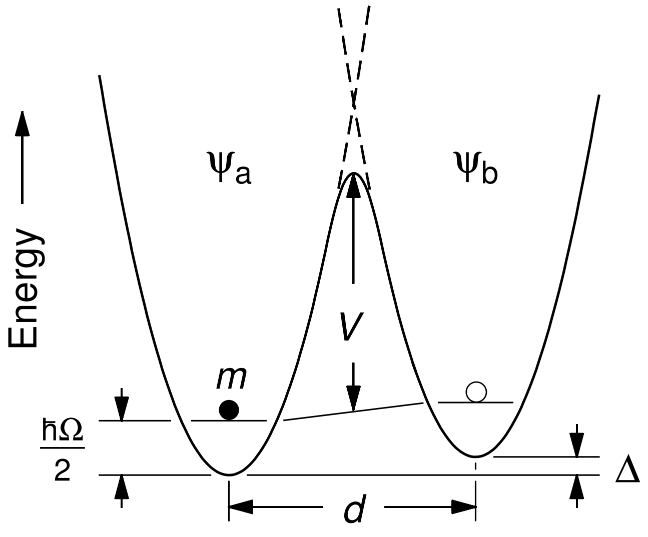

Fig. 2.5. Sketch of a double well potential. The ground state energy of either single well is $\hbar\Omega/2$. Δ is the asymmetry energy, d the distance between the wells, and V the height of the potential barrier. (From Enss and Hunklinger (2000))

From probability considerations it follows that the most likely number of such adjacent potential minima is two. Such configurations are called *double well potentials*, and an example of these is depicted in Fig. 2.5. There, the potential created by the surrounding atoms is plotted versus a general configuration coordinate, which is to be understood as an "effective" coordinate summarizing the relative motion of all atoms involved in the dynamics of the system, and d is the distance between the two wells in regard to this coordinate. Similarly, the mass m represents an effective mass of the "particle" moving in the potential. V denotes the height of the barrier between the two minima, and ψ_a and ψ_b are the wave functions of the *ground states* of the particle in the left and right well, respectively. In general the two minima will have a potential difference of Δ, called the asymmetry energy.

At temperatures below 1 K, in either single well only the ground states ψ_a and ψ_b, respectively, are occupied, as the energy of the excited states is of the order of several 10 K. Moreover, transitions from one well to the other via thermal activation are extremely unlikely. Thus, any such transition can take place only by quantum-mechanically tunneling through the potential barrier. The task to be addressed in the following is to determine the wave functions and eigenenergies of such systems.

The Hamiltonian governing the dynamics of a system with a double well potential is

$$H = -\frac{\hbar^2}{2m}\,\frac{d^2}{dx^2} + V(x)\,, \tag{2.3}$$

where x represents the applicable general coordinate. The exact form of the potential $V(x)$ is to some extent arbitrary, as the potential present in an actual glass is not known. A possible choice is the arrangement of two neighboring harmonic potentials. (See Phillips (1981) for examples.)

The ground state wave functions ψ_a and ψ_b of the single wells depend on the choice of the potential $V(x)$ and, for a sufficiently simple shape of the well, can be easily calculated. The wave function ψ of the particle in the double well potential is assumed to be, to a good approximation, a linear superposition of ψ_a and ψ_b, i.e.,

$$\psi = a\,\psi_a + b\,\psi_b\,, \tag{2.4}$$

where a and b are real-valued parameters that need to be determined. The energy of the system can be written as

$$E = \frac{\int \psi^* H \psi \, dV}{\int \psi^* \psi \, dV} = \frac{a^2 H_{aa} + b^2 H_{bb} + 2ab\, H_{ab}}{a^2 + b^2 + 2ab\, S}\,, \tag{2.5}$$

with $H_{ij} = \int \psi_i^* H \psi_j \, dx$ and $S = \int \psi_a^* \psi_b \, dx$, where the latter is the so-called overlap integral. Here, the Rayleigh-Ritz variational method is applied: for the ground state ψ, E should reach its minimum, i.e., $\delta E/\delta\psi = 0$. Differentiating E with respect to a and b, respectively, yields that E will be minimal for

$$(H_{aa} - E)(H_{bb} - E) - (H_{ab} - ES)^2 = 0\,. \tag{2.6}$$

The overlap integral S turns out to be small, and it can be approximated by $S = 0$. If we choose the zero of energy to be at the mean of the two single wells' ground states, it is found that $H_{aa} = +\mathit{\Delta}/2$ and $H_{bb} = -\mathit{\Delta}/2$. The value of the exchange integral H_{ab} depends on the assumptions that have been made regarding the shape of the barrier separating the two wells (see Phillips (1981)). As the details of the potential are not known, one often uses an expression reflecting the common characteristics of most barrier shapes, which describes the energy splitting due to the tunneling of the "particle" between the two wells as

$$\mathit{\Delta}_0 = \hbar \mathit{\Omega}\, \mathrm{e}^{-\lambda}\,. \tag{2.7}$$

The quantity $\mathit{\Delta}_0$ is called the tunnel splitting, and $\lambda = d\sqrt{2mV/\hbar^2}$ denotes the tunneling parameter, which reflects the overlap of the wave functions ψ_a and ψ_b. With this, one obtains $H_{ab} = -\mathit{\Delta}_0/2$, and can write the Hamiltonian in the basis $\{\psi_a, \psi_b\}$ as

$$H' = \frac{1}{2}\begin{pmatrix} \mathit{\Delta} & -\mathit{\Delta}_0 \\ -\mathit{\Delta}_0 & -\mathit{\Delta} \end{pmatrix}. \tag{2.8}$$

Now, solving Eq. (2.6) is equivalent to diagonalizing Eq. (2.8), which yields the two energy levels

$$E_\pm = \pm\frac{1}{2}\sqrt{\mathit{\Delta}^2 + \mathit{\Delta}_0^2}\,, \tag{2.9}$$

and we can write the Hamiltonian in the basis of its eigenfunctions $\{\psi_+, \psi_-\}$ as

$$\mathcal{H} = \frac{1}{2}\begin{pmatrix} E & 0 \\ 0 & -E \end{pmatrix}, \tag{2.10}$$

with the two-level system's energy splitting

$$E = E_+ - E_- = \sqrt{\mathit{\Delta}^2 + \mathit{\Delta}_0^2}\,. \tag{2.11}$$

Later, we will call each of these double well potential systems a "Two-Level System" (TLS), or a "Tunneling System" (TS).

2.2.2 Ensemble of Identical Tunneling Systems

For calculating the scattering rate between TLSs and phonons, we will review the occupation numbers of the energy levels of the TLSs in this section. For an ensemble of identical two-level systems with energy levels $E_\pm = \pm\frac{1}{2}\,E$, the partition function is

$$Z = \mathrm{e}^{-E_+/k_\mathrm{B}T} + \mathrm{e}^{-E_-/k_\mathrm{B}T} \tag{2.12}$$

and the occupation probability of either energy level is expressed by

$$p(E_\pm) = \frac{1}{Z}\,\mathrm{e}^{-E_\pm/k_\mathrm{B}T}\,. \tag{2.13}$$

From this it follows that for a TLS of energy splitting E the average occupation number of the upper level, with energy $E_+ = E/2$, is

$$f_{\mathrm{TLS}}(E) = p(+\frac{1}{2}E) = \frac{1}{\mathrm{e}^{E/k_{\mathrm{B}}T} + 1} \tag{2.14}$$

and the average occupation difference between the two levels is calculated to be

$$\varDelta p = p(E_-) - p(E_+) = \frac{\mathrm{e}^{E/2k_{\mathrm{B}}T} - \mathrm{e}^{-E/2k_{\mathrm{B}}T}}{\mathrm{e}^{E/2k_{\mathrm{B}}T} + \mathrm{e}^{-E/2k_{\mathrm{B}}T}} = \tanh\left(\frac{E}{2k_{\mathrm{B}}T}\right). \tag{2.15}$$

2.2.3 Tunneling Systems in Glasses

In a glass one will not find an ensemble of identical tunneling systems, rather will the double-well potentials have a broad distribution in their parameters. It is an important assumption of the Standard Tunneling Model that the tunneling parameter $\lambda = \ln(\hbar\varOmega/\varDelta_0)$ and the asymmetry energy $\varDelta$ are independent of each other, and have a uniform distribution, i.e.,

$$P(\varDelta, \lambda)\, d\varDelta\, d\lambda = \overline{P}\, d\varDelta\, d\lambda\,, \tag{2.16}$$

where $\overline{P}$ is a constant. The range of tunneling parameters is bounded, such that $\lambda_{\mathrm{min}} < \lambda < \lambda_{\mathrm{max}}$. The reason for having a lower bound is obvious, as for a given energy E, the largest value of the tunnel splitting is $\varDelta_0 \to E$, when the asymmetry $\varDelta \to 0$. Thus, $\lambda_{\mathrm{min}}(E) = \ln(\hbar\varOmega/E)$. The upper bound λ_{max} will be explained below.

To discuss this, it is convenient to rewrite Eq. (2.16) in terms of E, employing the expression in Eq. (2.11), so that the distribution function reads

$$P(E, \lambda)\, dE\, d\lambda = \overline{P} \frac{E\, dE\, d\lambda}{\sqrt{E^2 - (\hbar\varOmega\, \mathrm{e}^{-\lambda})^2}}\,. \tag{2.17}$$

Integration over all values of the tunneling parameter λ yields the density of states

$$D_{\mathrm{TLS}}(E) = \int\limits_{\lambda_{\mathrm{min}}(E)}^{\lambda_{\mathrm{max}}} P(E, \lambda)\, d\lambda = \overline{P}\, \ln\left(\frac{2\,E}{\varDelta_{0,\mathrm{min}}}\right). \tag{2.18}$$

Here the need to have an upper bound $\lambda_{\mathrm{max}} = \ln(\hbar\varOmega/\varDelta_{0,\mathrm{min}})$ becomes evident, as the integral will not converge otherwise. Also, in any finite volume of glass the number of tunneling systems is finite, which implies the existence of a boundary $\lambda_{\mathrm{max}} < \infty$ for the tunneling parameter.

From Eq. (2.18), we know that the density of states can be regarded as a constant, $D_{\mathrm{TLS}}(E) \simeq D_0$, if $\varDelta_{0,\mathrm{min}}$ is proportional to E. Hunklinger and Raychaudhuri (1986) have estimated an upper limit of $\varDelta_{0,\mathrm{min}}/E \simeq 10^{-6}$ from the results of “thermal relaxation” experiments. Whether any stricter limits can be specified is an issue that is still investigated.

2.2.4 Interaction of TLSs with Phonons

The two-level systems interacts with elastic strain fields in the solid. This mechanism provides the means for an energy exchange between phonons and defects, in which a two-level system can change its state from one level to the other. One typically assumes that this interaction is small compared to the eigenenergy of the tunneling system, i.e. the changes it causes to the parameters $\varDelta$ and $\varDelta_0$ can be treated with first-order perturbation theory. The Hamiltonian including the perturbation in the basis $\{\psi_a, \psi_b\}$ reads

$$H' = H'_0 + H'_1 = \frac{1}{2}\begin{pmatrix} \varDelta & -\varDelta_0 \\ -\varDelta_0 & -\varDelta \end{pmatrix} + \frac{1}{2}\begin{pmatrix} \delta\varDelta & -\delta\varDelta_0 \\ -\delta\varDelta_0 & -\delta\varDelta \end{pmatrix}. \tag{2.19}$$

The variation of the tunnel splitting $\delta\varDelta_0$ is usually assumed to be negligible (see Phillips (1981) for elaboration). The change in the asymmetry energy due to the interaction with the distortion of the lattice is to first order

$$\delta\varDelta = 2\,\gamma\,\tilde{e}\,, \tag{2.20}$$

where γ represents the deformation potential and $\tilde{e}$ the elastic strain. (Due to the polarization of the strain field, both quantities are in fact tensors, but here they will be treated as scalars for simplicity.) In the basis of the eigenstates $\{\psi_+, \psi_-\}$ of H'_0, the Hamiltonian is then written as

$$\mathcal{H} = \mathcal{H}_0 + \mathcal{H}_1 = \frac{1}{2}\begin{pmatrix} E & 0 \\ 0 & -E \end{pmatrix} + \frac{\gamma\tilde{e}}{E}\begin{pmatrix} \varDelta & \varDelta_0 \\ \varDelta_0 & -\varDelta \end{pmatrix}. \tag{2.21}$$

In a complete treatment of this problem (see Jäckle, Piché, Arnold, and Hunklinger (1976) and Hunklinger and Arnold (1976)), a formal analogy is established between the Hamiltonian in Eq. (2.21) and the one describing the motion of a spin $\frac{1}{2}$ particle in a static magnetic field with an oscillatory perturbing field. It is found that the interaction between the localized tunneling states and the phonon field results in two distinct contributions to the sound dispersion and absorption. One is due to the resonant interaction between the sound wave and the two-level systems, and the other has the typical form of a relaxation process. These two processes can be treated independently.

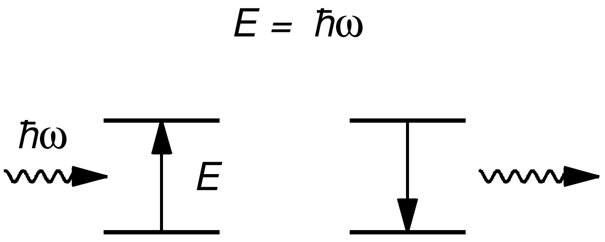

Fig. 2.6. One-phonon, or direct process. The transition from one energy level to the other is performed via absorption or emission of a phonon of energy $\hbar\omega$.

When examining this interaction at temperatures below 1 K, only the one-phonon, or direct process needs to be taken into account, as processes involving two or more phonons are very unlikely at such low temperatures. As shown in Fig. 2.6, in the direct process a tunneling system interacts with a phonon whose frequency ω corresponds to the TLS's energy splitting E.

The timescales of the relaxation and resonance processes are expressed by means of the respective rates, which can be calculated employing Fermi's Golden Rule (Jäckle 1972). The quantity $\tau^{-1}_{\alpha,\mathrm{res}}$ characterizes the rate, at which a phonon with polarization α, sound velocity v_α, and momentum $k = \omega/v_\alpha$ is absorbed by a TLS with energy splitting $E = \hbar\omega$, i.e., with which the phonon is at resonance, and it reads

$$\tau_{\alpha,\mathrm{res}}^{-1} = \frac{2\pi}{\hbar} \int dE \;\, V D_{\mathrm{TLS}}(E)\, \mathit{\Delta} p(E)\; |\langle \psi_+ | \mathcal{H}_1 | \psi_-; k, \alpha \rangle|^2 \;\, \delta(E - \hbar\omega)\,, \tag{2.22}$$

where V is the volume of the glass sample. The matrix element for absorption or emission of a phonon with momentum k and polarization α can be expressed as (Kittel 1963, Jäckle 1972)

$$\langle \psi_+ | \mathcal{H}_1 | \psi_-; k, \alpha \rangle = \sqrt{\frac{\hbar k}{2V\,\rho v_\alpha}}\; \gamma_\alpha \, \frac{\mathit{\Delta}_0}{E}\,. \tag{2.23}$$

Hence, the scattering rate $\tau_{\alpha,\mathrm{res}}^{-1}$ is greatest when the asymmetry energy $\mathit{\Delta}$ is zero, i.e., for $E = \mathit{\Delta}_0$. Using the constant density of states of the TLSs, $D_{\mathrm{TLS}}(E) \simeq D_0$, and the associated difference in occupation probability given in Eq. (2.15), the scattering rate $\tau_{\alpha,\mathrm{res}}^{-1}$ can then be written as

$$\tau_{\alpha,\mathrm{res}}^{-1} = \frac{\gamma_\alpha^2 D_0}{\rho v_\alpha^2}\, \pi\omega \, \tanh\left(\frac{\hbar\omega}{2k_{\mathrm{B}}T}\right). \tag{2.24}$$

In ultrasonic experiments on amorphous materials, the resonant interaction between phonons and TLSs is only responsible for the absorption at low sound intensities I. For intensities above a certain critical level, $I > I_{\mathrm{c}}$, this absorption saturates as the two energy levels of the tunneling systems become equally populated, i.e., $\mathit{\Delta} p \simeq 0$.

Equation (2.24) also describes the interaction of the thermal phonons with the TLSs. Hence, in the following section, an expression for the thermal conductivity of amorphous substances will be derived from the rate of resonant scattering $\tau_{\alpha,\mathrm{res}}^{-1}$.

In contrast to this, relaxation processes occur when an ultrasonic wave creates a perturbation which brings the TLSs out of thermal equilibrium. The relaxation rate of a TLS, τ_{rel}^{-1}, quantifies the timescale on which a specific TLS with energy splitting E will return to its ground state after an excitation. It is calculated as

$$\tau_{\mathrm{rel}}^{-1} = \frac{2\pi}{\hbar} \sum_{\alpha = l,t,t} \int d(\hbar\omega)\; V D_{\alpha,\mathrm{ph}}(\hbar\omega)\; \big[1 + 2 f_{\mathrm{ph}}(\hbar\omega)\big]\; |\langle \psi_+ | \mathcal{H}_1 | \psi_-; k, \alpha \rangle|^2 \;\, \delta(E - \hbar\omega)\,. \tag{2.25}$$

The factor $\big(1 + 2f_{\mathrm{ph}}(\hbar\omega)\big)$ is composed of $\big(1 + f_{\mathrm{ph}}(\hbar\omega)\big)$ for the creation and $f_{\mathrm{ph}}(\hbar\omega)$ for the annihilation of a phonon. The Debye approximation for the phonon density of states per unit volume is

$$D_{\alpha,\mathrm{ph}}(\hbar\omega) = \frac{D_{\alpha,\mathrm{ph}}(\omega)}{\hbar} = \frac{\omega^2}{2\pi^2\hbar}\, \frac{1}{v_\alpha^3}\,, \tag{2.26}$$

with the polarization-dependent velocity of sound v_α. The phonons obey the Bose-Einstein distribution which reads

$$f_{\mathrm{ph}}(\omega) = \frac{1}{\mathrm{e}^{\hbar\omega/k_{\mathrm{B}}T} - 1}\,. \tag{2.27}$$

Having inserted these quantities, and after summing over all polarizations α, we obtain the relaxation rate for TLSs with energy splitting E as

$$\tau_{\mathrm{rel}}^{-1} = \left(\frac{\gamma_{\mathrm{l}}^2}{v_{\mathrm{l}}^5} + \frac{2\,\gamma_{\mathrm{t}}^2}{v_{\mathrm{t}}^5}\right)\left(\frac{\varDelta_0}{E}\right)^2 \frac{E^3}{2\pi\rho\,\hbar^4}\coth\left(\frac{E}{2k_{\mathrm{B}}T}\right). \tag{2.28}$$

Note that for a given energy E, the rate τ_{rel}^{-1} depends on the square of the ratio $\varDelta_0/E$. Again, the relaxation rate is maximal for those TLSs which have $\varDelta_0 = E$, i.e., whose asymmetry is zero.

In the experiment to be described in this work, this distribution of relaxation times results in a "heat release" within the sample. This requires the experimenter to wait for a considerable period of time for the sample to thermalize at low temperature before performing measurements on it.

2.3 Predictions of the Standard Model

Now we will use the formalism of the Standard Tunneling Model developed in the previous section to derive expressions for the thermal properties of amorphous solids.

2.3.1 Thermal Conductivity

It was shown by Zaitlin and Anderson (1975) that the heat transport in amorphous solids below about 20 K is carried out by phonons. Hence, the thermal conductivity κ is derived by employing the kinetic formula

$$\kappa(T) = \frac{1}{3}\sum_{\alpha}\int_0^{\omega_{\mathrm{D}}} C_\alpha(\omega)\, l_\alpha(\omega)\, v_\alpha(\omega)\, d\omega\,. \tag{2.29}$$

Here $\omega_{\mathrm{D}} = k_{\mathrm{B}}\varTheta_{\mathrm{D}}/\hbar$ is the "Debye frequency", derived from the glass's "Debye temperature" $\varTheta_{\mathrm{D}}$, as outlined in Freeman and Anderson (1986). At low temperature, $\hbar\omega_{\mathrm{D}}$ is much higher than the energies of the thermal phonons present in the glass. Therefore, the upper bound can be set to infinity. (For the value of the Debye temperature in some typical glasses, see Table 2.1.) The quantity $C_\alpha(\omega)$ is the specific heat of the phonons with polarization α and energy $\hbar\omega$. The quantity $l_\alpha(\omega)$ is the mean free path, and $v_\alpha(\omega)$ the velocity of these phonons.

Using the phonons' density of states and distribution in equations (2.26) and (2.27), respectively, we find that

$$C_\alpha(\omega) \;=\; \hbar\omega\, D_{\alpha,\mathrm{ph}}(\omega)\,\frac{df_{\mathrm{ph}}(\omega)}{dT} \;=\; \frac{\omega^2}{2\pi^2}\,\frac{k_{\mathrm{B}}}{v_\alpha^3}\,\frac{x^2\,\mathrm{e}^x}{(\,\mathrm{e}^x-1)^2}\,, \tag{2.30}$$

where we have introduced the substitution $x = \hbar\omega/k_{\mathrm{B}}T$, which will also be used in the following.

For the phonons' mean free path, using the rate of resonant scattering $\tau_{\alpha,\mathrm{res}}^{-1}$ given in Eq. (2.24), we have

$$l_\alpha^{-1}(\omega) \;=\; \frac{\tau_{\alpha,\mathrm{res}}}{v_\alpha} \;=\; \frac{\gamma_\alpha^2 D_0}{\rho v_\alpha^3}\,\pi\omega\,\tanh\left(\frac{\hbar\omega}{2k_{\mathrm{B}}T}\right). \tag{2.31}$$

It can be shown that the variation of the sound velocity $\delta v_\alpha / v_\alpha$ at low temperature has about the magnitude $\gamma_\alpha^2 \, D_0 / \rho v_\alpha^2 \cdot \ln(T/T_0)$, with some reference temperature T_0 (Piché, Maynard, Hunklinger, and Jäckle 1974). For most amorphous materials, the value $\gamma_\alpha^2 \, D_0 / \rho v_\alpha^2$ is of the order 10^{-4}. This results in a change of the sound velocity of $\lesssim 0.1$ % from 1 mK to 0.1 K. (Experimental results from Classen, Burkert, Enss, and Hunklinger (2000) showed a relative change $\delta v_\alpha / v_\alpha$ of $\lesssim 0.1$ % for the temperature range from 5 mK to 1 K.) Hence, in the following we may simply regard the sound velocity v_α as constant.

Inserting appropriate quantities into the kinetic formula in Eq. (2.29), we obtain an expression for the thermal conductivity, which reads

$$\kappa(T) = \frac{\rho \, k_\mathrm{B}^3 \, T^2}{6\pi^3 \hbar^2} \left(\frac{v_\mathrm{l}}{D_0 \, \gamma_\mathrm{l}^2} + \frac{2 \, v_\mathrm{t}}{D_0 \, \gamma_\mathrm{t}^2} \right) \cdot \int\limits_0^\infty \frac{x^3 \, \mathrm{e}^x (\, \mathrm{e}^x + 1)}{(\, \mathrm{e}^x - 1)^3} \, dx \, , \tag{2.32}$$

where the upper bound in the integration has been replaced by infinity. The integral evaluates to π, hence we arrive at the formula

$$\kappa(T) = \frac{\rho \, k_\mathrm{B}^3 \, T^2}{6\pi^2 \hbar^2} \left(\frac{v_\mathrm{l}}{D_0 \, \gamma_\mathrm{l}^2} + \frac{2 \, v_\mathrm{t}}{D_0 \, \gamma_\mathrm{t}^2} \right) . \tag{2.33}$$

Especially noteworthy in this result is that it predicts a T^2 dependence of the thermal conductivity, as it has also been found experimentally.

2.3.2 Specific Heat

In addition to the specific heat of the phonon gas, in glasses there is an "excess" contribution arising from the two-level systems. This contribution can be derived from the formula

$$C_\mathrm{TLS}(T) = \frac{d}{dT} \int\limits_0^\infty E \, D_\mathrm{TLS}(E) \, f_\mathrm{TLS}(E) \, dE \, . \tag{2.34}$$

With the tunneling systems' density of states and average occupation probability from equations (2.18) and (2.14), respectively, and the substitution $x = E / k_\mathrm{B} T$, it then follows that

$$C_\mathrm{TLS}(T) = k_\mathrm{B}^2 \, D_0 \, T \cdot \int\limits_0^\infty \frac{x^2 \, \mathrm{e}^x}{(\, \mathrm{e}^x + 1)^2} \, dx \, . \tag{2.35}$$

The integral evaluates to $\pi/6$, and we obtain the tunneling systems' "excess" specific heat as

$$C_\mathrm{TLS}(T) = \frac{\pi}{6} \, k_\mathrm{B}^2 \, D_0 \, T \, . \tag{2.36}$$

This equation predicts a linear dependence of the amorphous solid's additional heat capacity C_TLS on the temperature, close to the behavior that has been found experimentally (see section 2.1.1).

On a side note, it has so far not been taken into account that, in a measurement of the specific heat, only those TLSs whose relaxation time τ_{rel} is shorter than the duration of the measurement, can contribute to the experimental results. When taking into account this time dependence, the specific heat due to the TLSs is calculated as (Black 1978)

$$C_{\text{TLS}}(T,t) \simeq \frac{\pi^2}{12}\, k_{\text{B}}^2 T D_0 \, \ln\left(66.24 A\, T^3 t\right) , \quad \text{with } A = \frac{1}{2\pi\rho\hbar^4}\left(\frac{\gamma_{\text{l}}^2}{v_{\text{l}}^5} + \frac{2\,\gamma_{\text{t}}^2}{v_{\text{t}}^5}\right) . \tag{2.37}$$

However, by interpreting the results from heat capacity measurements in the framework of a thermodynamic field theory, it is possible to derive an expression for the specific heat of glasses that is not time-dependent (Strehlow and Meissner 1999).

In contrast to the linear term of the specific heat, the Standard Tunneling Model does not explain the "excess" cubic term of the specific heat in Eq. (2.1), which is also characteristic for amorphous materials. It has been found experimentally that, unlike the linear term, this excess cubic term shows no time dependence (Hunklinger and Raychaudhuri 1986). This demonstrates that the underlying excitations are due to another mechanism, which so far has not been explained conclusively.

2.4 Interactions between Two-Level Systems

The Standard Tunneling Model's success in describing the low temperature properties of amorphous materials is quite remarkable, especially when considering that it is based on relatively simple assumptions and, moreover, does not make any specification to the identity of the tunneling states it proposes. However, there are several experimental results that indicate that the Standard Model cannot completely describe the observations at very low temperature.

In an investigation of the dielectric constant of several kinds of glass (Salvino, Rogge, Tigner, and Osheroff 1994, Rogge, Natelson, and Osheroff 1996), and of the internal friction of vitreous silica (Classen, Burkert, Enss, and Hunklinger 2000), the temperature dependence observed at very low temperature was weaker than predicted by the Standard Model.

In another experiment measuring the dielectric constant, Strehlow, Enss, and Hunklinger (1998) observed a phase transition in multi-component glasses, in the case of barium aluminosilicate glass (BaO-Al_2O_3-SiO_2) at 5.84 mK. Below this temperature, the dielectric constant of the glass depends strongly on the magnitude of the magnetic field. Later it was found that there is also a magnetic field dependence of the dielectric properties of this glass above the transition temperature, even though the magnitude of this effect is considerably weaker (Strehlow et al. 2000). The origin of this magnetic field dependence has so far not been fully understood.

As the one-phonon process, which is the dominant process below 1 K, is gradually suppressed when cooling to very low temperatures, one would naturally assume that processes due to the interactions between the TLSs would gain in importance. Hence, deviations from the predictions of the Standard Model could be expected, as this model does not include the interactions that take place between the tunneling systems.

First evidence for the importance of such interactions came from acoustic "hole burning" experiments (Arnold and Hunklinger 1975). There, "spectral diffusion" effects occur (Black and Halperin 1977) which arise because of an elastic interaction between the tunneling states, mediated by phonons.

A theory made to explain the findings in dielectric constant and internal friction is the *Dipole Gap Model*, put forward by Burin (1995). This model assumes a resonant interaction between pairs of nearly degenerate TLSs, one of which is in its excited state. Below a certain cross-over temperature T_*, the relaxation rate of the relevant pairs, with excitation energies $E \simeq k_{\mathrm{B}}T$, surpasses the one-phonon process relaxation rate. Hence, for $T < T_*$, the pair interaction governs the dielectric and acoustic properties of the solid. In the literature, an estimate of the cross-over temperature $T_* \simeq 0.6$ mK is given for vitreous silica (Classen, Burkert, Enss, and Hunklinger 2000).

Within the dipole gap model, a phononless heat transport in amorphous solids, due to the interaction between the TLSs, is predicted (Burin, Maksimov, and Polishchuk 1989). The contribution of this mechanism to the thermal conductivity assumes the form $\kappa_{\mathrm{TLS}} \propto T^{4/3}$. Here, the cross-over temperature T_* is reached when this contribution due to the tunneling states becomes comparable in magnitude to the phononic heat conduction, i.e., $\kappa_{\mathrm{ph}} \simeq \kappa_{\mathrm{TLS}}$. For dielectric glasses, a transition temperature far below 1 mK is predicted (Kagan, Maksimov, and Polishchuk 2000).

In an extension of the dipole gap model, Würger and Bodea (2003) have undertaken a theoretical investigation into the possibility of heat conduction due to clusters of almost degenerate, weakly interacting TLSs. This approach, too, yields a contribution to the thermal conductivity of the form $\kappa_{\mathrm{TLS}} \propto T^{4/3}$. In the Millikelvin range, however, the heat transport carried out by TLSs is predicted to be smaller by many orders of magnitude than the phononic thermal conductivity.

This is in agreement with the fact that to date, in all heat transport measurements performed on amorphous solids at very low temperature, the observed behavior of the thermal conductivity is of the form $\kappa(T) \propto T^{\eta}$, with $\eta = 1.7 - 2$. Even recent experiments undertaken by Rosenberg, Natelson, and Osheroff (2000), despite having reached temperatures as low as 10 mK, did not show distinct deviations from the predictions of the Standard Tunneling Model. To the lowest temperatures, their measured thermal conductivity scaled approximately as $T^{1.85}$, close to the T^2 dependence derived by the Standard Model.

All experimental methods developed so far to investigate the low temperature heat transport in amorphous materials are only applicable at temperatures above 10 mK. As there is both experimental and theoretical evidence for the growing importance of interaction between tunneling states in the low Millikelvin temperature range, it is clearly desirable to develop a method for measurements at lower temperature. In this work, a contact-free measurement technique is introduced. Results of measurements performed on different species of glass samples in the temperature range down to 5 mK are presented.

3. Experimental Technique

3.1 Introduction

At very low temperature, performing a thermal conductivity measurement on amorphous samples is a challenging task for several reasons. First, glasses have poor thermal conductivity, so the heat input $\dot{Q}$ required for the measurement is very small. This sets a strict limit to the parasitic heat input that is tolerable in such an experiment. Moreover, the heat capacity of the system decreases with decreasing temperature, aggravating matters further as already a small heat leak into the setup may considerably disturb the temperature in the sample.

In a setup with traditional thermometers and a resistance heater, the electrical leads required for operation represent the prime source of heat leaks. This problem can be partially overcome; superconductive wires may be used which, below their critical temperature T_{c}, have only a small thermal conductivity. Also, the wires can be thermally anchored at various temperature stages, which will further reduce the parasitic heat input into the system. However, this might lead to the converse problem of heat shunts.

With a wire-based setup, undesired heating can be introduced by the measurement devices. Care has to be taken that these devices and the cryostat have a common electrical ground in order to avoid ground currents. Also, filters have to be installed to reduce heating due to radio-frequency noise. Even more serious, though, is the self-heating effect within the thermometers, as the latter do need a certain minimum current in order to operate.

Thus, for thermal conductivity measurements at very low temperature, it is desirable to minimize the number of electrical leads connecting to the sample, and to develop a thermometry technique which dissipates only an extremely small amount of power.

In a recent experiment, Rosenberg, Natelson, and Osheroff (2000) have successfully measured the thermal conductivity of the borosilicate glass BK7 down to about 10 mK. There, the dielectric constant of the sample itself was used for thermometry. This technique has a very low power dissipation of about 0.1 pW, and has the additional advantage of having no boundary resistance between the thermometers and the sample. However, despite considerable precautions to reduce heat leaks, a residual dissipation of about 1 pW remained, limiting reliable measurements to temperatures above 10 mK.

In this work, we present a measurement technique that entirely avoids electrical contacts to the sample. Heating is accomplished optically, and a SQUID[1]-based paramagnetic thermometry has been implemented, which facilitates a highly sensitive temperature measurement while causing only very little undesired heating on the sample.

---

[1] Superconductive Quantum Interference Device

3.2 Low Temperature Environment

3.2.1 Dilution Refrigerator

The ^{3}*He*-^{4}*He dilution refrigerator* is a cooling device which generates temperatures down to the low Millikelvin range. This cooling technique has been discussed extensively in the literature (see e.g. Pobell (1992), and Enss and Hunklinger (2000)). Therefore, only a brief sketch of the operating principle of the cryostat will be given here.

At temperatures above 0.87 K, the two liquids ^{3}He and ^{4}He can be mixed in arbitrary ratios. Below this temperature, a separation in two phases occurs, with one rich in ^{3}He, and the other rich in ^{4}He. For $T \to 0$, the ^{3}He-rich mixture simply turns into pure ^{3}He. The ^{4}He-rich phase, however, contains 6.6 % of ^{3}He even at absolute zero, rather than becoming a pure superfluid ^{4}He phase, as it might be expected.

Like using the latent heat of evaporation, this property of ^{3}He-^{4}He mixtures can be utilized in a cooling technique, as first proposed by London, Clarke, and Mendoza (1962). The enthalpy of a ^{3}He atom is larger in the ^{3}He-^{4}He mixed phase than in the pure ^{3}He phase. Thus, when ^{3}He atoms are transferred from the pure ^{3}He phase to the diluted, mostly ^{4}He-containing phase, heat needs to be extracted from the liquids, which leads to the cooling effect. A consequence of the finite solubility of ^{3}He in ^{4}He is that the cooling power has a weaker temperature dependence in this dilution process than it does in the evaporation process. Hence, with a dilution refrigerator, lower temperatures can be reached.

Figure 3.1 shows a schematic of the dilution refrigerator operated in our laboratory. The boundary between the two phases of ^{3}He and ^{3}He-^{4}He mixture is located in the *mixing chamber*. Due to the cooling associated with the crossing of the boundary by ^{3}He atoms, the mixing chamber is the coldest part of the cryostat. In order to extract ^{3}He from the mixed phase, a volume containing a mixture of less than 1 % ^{3}He concentration, which is called the *still*, is connected to the mixed phase in the mixing chamber. An osmotic pressure arising due to the concentration difference will "pump" the ^{3}He atoms from the mixing chamber. The still itself is pumped by a vacuum pump and maintained at a temperature around 0.7 K.

On the condensing side, the returning ^{3}He is precooled while flowing through the liquid helium (LHe) bath, and is then brought in thermal contact with the 1 *K-pot*, which is a small ^{4}He bath that is pumped upon, and thus kept at a temperature of about 1.5 K. There, the ^{3}He condenses. After passing an impedance that maintains the pressure required for the condensation process, it is cooled further at the still. The last precooling process is accomplished by means of several heat exchangers, where the incoming ^{3}He transfers some of its thermal energy to the cold outgoing mixture, and after that returns into the pure ^{3}He liquid phase without introducing much heat into the mixing chamber.

The dilution refrigerator used for this experiment has a base temperature of about 5 mK. The experimental setup designed for the measurement of thermal conductivities is mounted on a copper plate thermally coupled to the mixing chamber. Two SQUIDs used for our thermometry technique are located at the 1 K-pot; they obtain their input signals through flux transformers

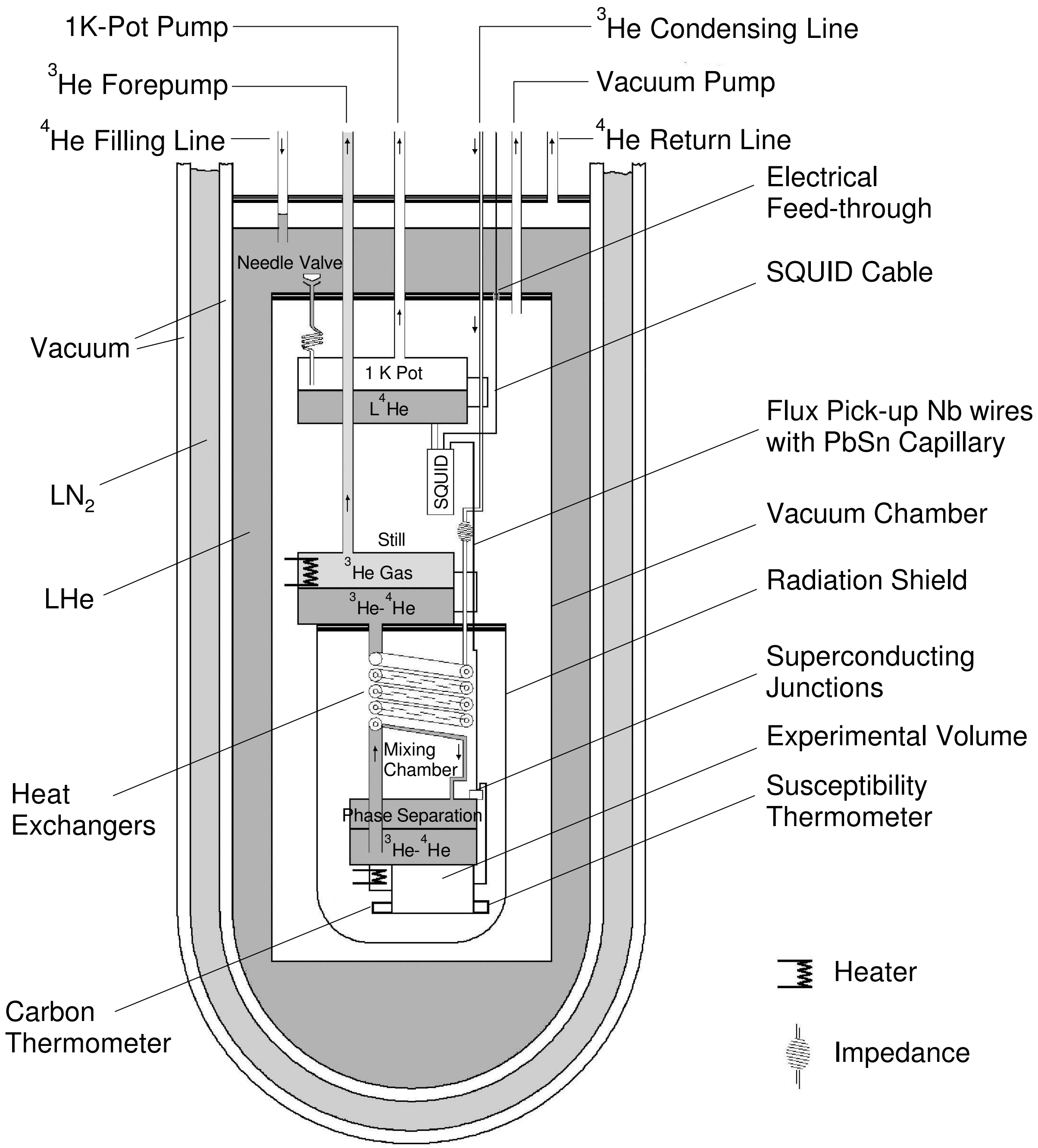

Fig. 3.1. Schematic of the dilution refrigerator used in this work.

going down to the setup at the mixing chamber. The experimental setup will be described in detail in a later section.

In the next sections, we will briefly describe the two thermometers which provide the information about the mixing chamber temperature that is needed for temperature regulation, and for carrying out the experiment.

3.2.2 Carbon Resistance Thermometer

This type of thermometer, widely used in low temperature experiments, utilizes the temperature dependence of the resistivity of commercial carbon resistors. The specimen used in our cryostat was manufactured in the research group of K. Neumaier at the Walther-Meißner Institute in Munich (Eska and Neumaier 1983). There, it was calibrated for the temperature range between 18 mK and 4 K. Figure 3.2 displays the resistor's temperature characteristics. As shown in the figure, the original resistance-temperature calibration curve has been extrapolated to temperatures reaching down to 5 mK (Weis 1995).

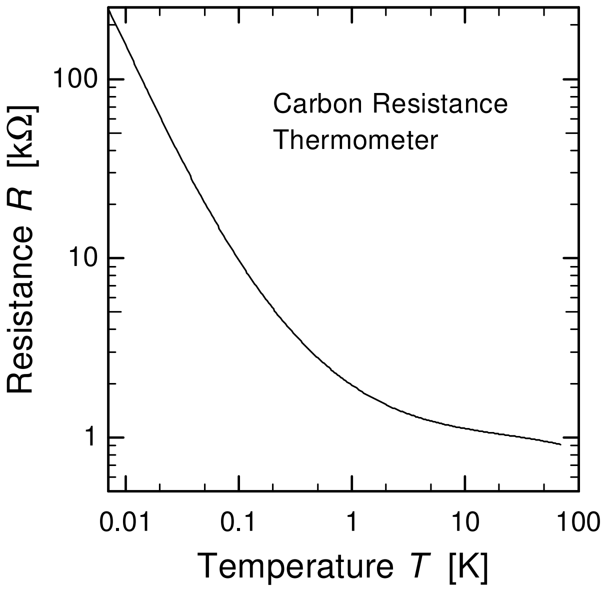

Fig. 3.2. Temperature dependence of the resistor in the carbon thermometer used in the present experiment (from Weis (1995)).

In order to account for possible changes in the resistance's temperature dependence over time, and to verify that temperature readings were accurate also in the extended temperature range below 18 mK, the calibration of the carbon thermometer in its present environment was compared to a ^{60}Co nuclear orientation thermometer by Fleischmann (1998). The result of that procedure confirmed that the carbon thermometer's temperature readings at 5 mK were accurate within about 5 %.

The specific carbon resistance thermometer used here features a good thermal coupling to the mixing chamber, and thus has a very fast response time, and does not show signs of saturation. However, towards lower temperatures, i.e., below 15 mK, the statistical error in its temperature readings increases drastically. This is due to the fact that the resistance of the thermometer rises rapidly with decreasing temperature, as seen in Fig. 3.2, which leads to a signal with high noise level. For accurate temperature values, averaging over significant time intervals is necessary. Hence, for tasks that require temperature readings with great stability, such as regulating the mixing chamber temperature, another type of thermometer is used, which will be described in the following section.

3.2.3 Paramagnetic Susceptibility Thermometer

For a paramagnetic material, the magnetic susceptibility varies with temperature according to the Curie-Weiss law

$$\chi = \frac{C}{T - T_{\mathrm{c}}}, \quad \text{for } T > T_{\mathrm{c}}, \tag{3.1}$$

where T_{c} is called the Curie temperature, and C the Curie constant. Hence, in paramagnetic susceptibility thermometry, the temperature of a paramagnetic sensor is determined by measuring its magnetization.

For the susceptibility thermometer used in our cryostat, this task is performed with an inductance bridge. (A more sensitive measurement technique involving the use of SQUIDs will be presented in section 3.3.1.) The thermometer consists of a primary coil and two secondary coils. As shown in Fig. 3.3, one of the secondary coils is wound upon the paramagnetic sensor. The other, as a background compensator, is identical to the former in geometry, but counter-wound on a Macor tube. With the aid of the LR-700 bridge[2], the mutual inductance between the primary coil and the secondary coils is measured. From this, the susceptibility of the sensor, and hence its temperature, are determined. For all details concerning the geometry of the setup and the readout electronics, see Horst (1999).

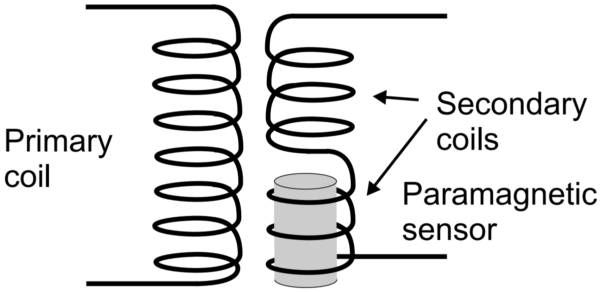

Fig. 3.3. Coil arrangement of the susceptibility thermometer. In the actual setup, the secondary coils are enclosed by the primary coil. Here they are drawn next to each other for clarity. (Horst 1999)

In the susceptibility thermometer described here, the sensor substance is a paramagnetic alloy. It consists of gold as host metal, and is doped with rare earth erbium. The advantage in using a metallic host is that, in contrast to paramagnetic salts such as Cerium-Magnesium Nitrate (CMN), it has a much faster response time. This is because it is much easier to create good thermal coupling to metals by clamping, and the much higher thermal conductivity of alloys leads to a fast thermalization of the sensor.

The amount of the erbium dopant to be introduced into the gold host has to be chosen to satisfy two conflicting requirements. To ensure a large signal-to-noise ratio in the inductance bridge, a high concentration of erbium ions is desirable. On the other hand, the interaction between the erbium ions prohibits the use of an arbitrarily large amount of dopant. At low temperature, a sensor with a higher concentration of Er will undergo a phase transition from a paramagnet to a spin-glass. In the latter phase, the magnetization of the Au:Er sensor becomes almost independent of temperature, such that it can no longer be used as a thermometer.

The sensor of the susceptibility thermometer used in this work has an erbium concentration of 1700 ppm. Its susceptibility-temperature characteristics is displayed in Fig. 3.4. At the lowest temperatures, the onset of a saturation becomes visible. Hence, calibrating the susceptibility thermometer by a fit to the Curie law described by Eq. (3.1) is not practical. Instead, the calibration

---

[2] LR-700 AC Resistance Bridge. Linear Research Inc., San Diego, California.

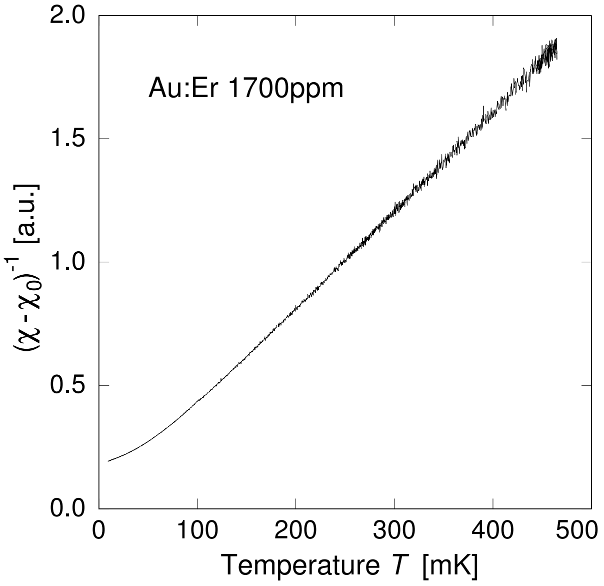

Fig. 3.4. Temperature dependence of the inverse magnetic susceptibility of a 1700 ppm Au:Er sample, used in the susceptibility thermometer in our cryostat's mixing chamber. χ_0 describes a background signal that does not vary with temperature (from Horst (1999)).

was performed by comparing its reading to the temperature obtained from the carbon resistance thermometer described in the previous section.

As apparent from the figure, the statistical noise in the susceptibility measurement decreases towards lower temperature, in contrast to the carbon thermometer. Due to its high stability, the susceptibility thermometer is used for regulating the mixing chamber temperature. This is essential for the thermal conductivity experiment, in which the temperature variation that is generated within the glass sample and needs to be measured, is less than 5 % of the ambient temperature.

Note that the temperature readings of the susceptibility thermometer are known to have small offsets ($< 10\,\%$ at 5 mK), which may even vary due to thermal cycling. Therefore, during our experiment the readings from the carbon thermometer were also recorded as a primary information for the temperature. Since the measuring time is usually quite long at low temperature, the carbon thermometer's readings can be averaged such that statistical noise is significantly reduced.

3.3 Thermal Conductivity Measurement

3.3.1 Measurement Principle

The principle of a thermal conductivity measurement is straightforward. In Fig. 3.5, a typical setup is sketched. A heater is attached to one end of the sample, while the sample's other end is thermally coupled to a reservoir at constant temperature T_{bath}. Between the two ends, two thermometers are attached to the sample at a specified distance L. When the heater dissipates a constant power $\dot{Q}$ into the sample, a temperature gradient between the two ends develops until a steady state is reached, i.e., until the temperature distribution within the sample is constant in time. If the temperature readings of the two thermometers are given by T_1 and T_2, the thermal conductivity is then found to be

$$\kappa = \frac{\dot{Q}}{A}\frac{L}{T_1 - T_2}\,, \tag{3.2}$$

where A denotes the cross-section of the sample.

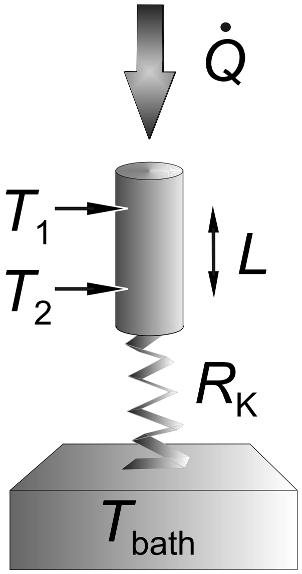

Fig. 3.5. Schematic of a thermal conductivity measurement.

It should be noted that the thermal coupling between the sample and the thermal bath is always imperfect. At low temperature, there exists a thermal boundary resistance at the interface of two materials, also denoted as the *Kapitza resistance* R_{K}, which causes a finite temperature difference between the two surfaces (Kapitza 1941, Swartz and Pohl 1989). If $\dot{Q}$ is the amount of heat flowing across the boundary per unit time, the temperature difference due to the Kapitza resistance is given by

$$\delta T = R_{\mathrm{K}}\dot{Q}\,. \tag{3.3}$$

The presence of a thermal boundary resistance will prolong the time for the glass sample to reach a steady state. Therefore it is advantageous to minimize R_{K} in the experimental setup. We will inspect this matter in section 4.5.

3.3.2 Experimental Setup

The experimental setup shown in Fig. 3.6 is mounted on the mixing chamber stage of a dilution refrigerator. The cylindrical glass sample is in tight fit with its copper holder, with STYCAST 1266 epoxy[3] used to fill any gaps between them. The copper holder has four slits cut along its length to compensate the tension due to the difference in thermal expansion between glass and copper. When using a holder without slits the glass sample broke in some cases. The sample holder is screwed down to the bottom plate of the mixing chamber with brass screws to ensure good thermal anchoring.

To provide the controlled heat input required in the measurement, we installed a light emitting diode (LED), with a room temperature peak wavelength of 623 nm, on a copper plate thermally

---

[3] STYCAST 1266. Emerson & Cuming Inc.

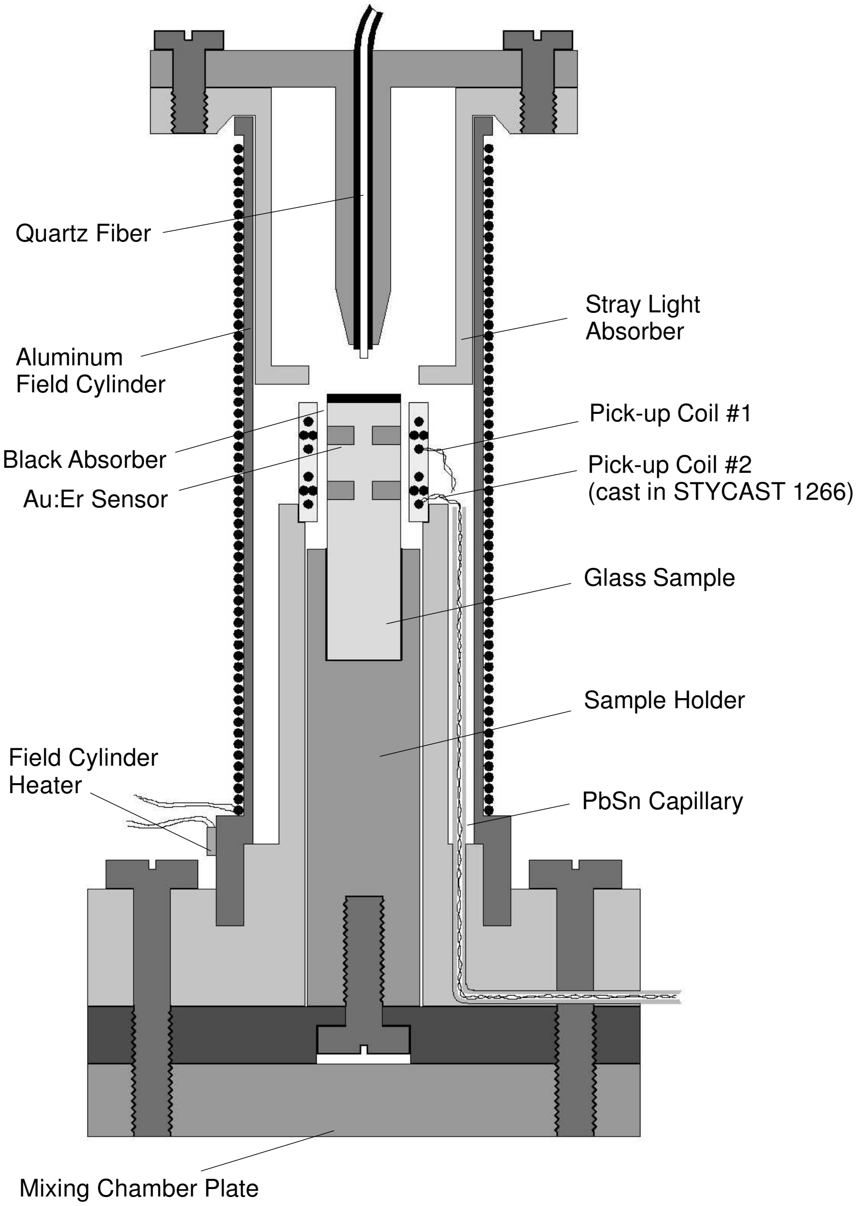

Fig. 3.6. Schematic of the experimental setup used to measure thermal conductivities. Heating is accomplished with the light output of an LED, which is transmitted through an optical quartz fiber, and absorbed by a black film attached to the sample's top end. Each of the superconducting wires coming from the pick-up coils around the Au:Er sensors leads to a SQUID, which translates the picked-up flux into a voltage signal. The setup is designed for cylindrical samples.

anchored at the 1 K-pot, and coupled it weakly to a single cord optical fiber which leads down to the sample at the mixing chamber plate. To prevent stray light from randomly heating any of the components of the cryostat, the LED is enclosed by a blackened metal capsule, and the optical fiber is shielded with black shrink tube. Moreover, in order to avoid direct heating of the Au:Er sensors, a stray light absorber with blackened interior is positioned under the fiber holder.

Since the light output of an LED has a nonlinear dependence on the driving voltage, we control the output by using a pulsed voltage signal of constant duration ($\sim 40\ \mu s$) and amplitude (~ 4 V). This way, the output power of the LED, $\dot{Q}_{\mathrm{LED}}$, is proportional to the repetition rate of the pulses, ν_{rep}, and so is the heat input $\dot{Q}$ used in the experiment, i.e., $\dot{Q} \propto \nu_{\mathrm{rep}}$. Furthermore, to enhance the stability of the current through the LED, on either side of the LED a 500 resistor is connected in series. The linearity of the heat input $\dot{Q}$ provided by this method has been examined and will be presented in section 4.2.

Here it should be mentioned that rf signals picked up by the electrical leads between LED and signal generator, or generated by the latter, do not lead to uncontrolled additional light output, as the LED's non-linear current-voltage characteristics has a steep onset at a voltage around 1.5 V.

In this experiment, we have used paramagnetic SQUID thermometers to measure the temperature gradient created by the heat input. The basic principle of this thermometry technique is the same as of the susceptibility thermometer described in section 3.2.3. However, instead of using a reactance bridge to measure the susceptibility of the paramagnetic sensors, a SQUID readout has been implemented to measure the magnetization of the sensors in a small constant magnetic field. This SQUID-based measurement technique is very sensitive, hence it is sufficient to use small amounts of sensor material, which at this time is an $\underline{\text{Au}}$:Er alloy with about 480 ppm of dopant.

In our experiment, we have used STYCAST 1266 epoxy to glue thin pieces of $\underline{\text{Au}}$:Er (~ 5.5 mm $\times$ 1 mm $\times$ 0.25 mm) onto the glass samples since the susceptibility of STYCAST 1266 is relatively small compared to other binding agents. The distance between the two temperature measuring points on the glass is only a few millimeters, hence the size of the $\underline{\text{Au}}$:Er pieces needs to be sufficiently small to obtain a well-defined local temperature. Besides, the specific heat of $\underline{\text{Au}}$:Er alloy is comparatively high in relation to the one of glass. Therefore, if the $\underline{\text{Au}}$:Er pieces are made too large, the time required by the system to reach a steady state will increase significantly.

As a device for flux detection, a SQUID magnetometer consists of a flux transformer and a dc SQUID with additional readout electronics. As flux pick-up loops for the SQUID magnetometer, two second-order gradiometers are wrapped with Nb wire of 200 µm diameter and cast in STYCAST 1266. Each gradiometer is situated in such a way that the corresponding $\underline{\text{Au}}$:Er pieces are aligned with its center. The reasons for using gradiometers, rather than simple loops, are twofold. A second-order gradiometer is more sensitive to a flux distribution which has a maximum at the middle of the gradiometer, hence flux pick-up from the non-corresponding set of $\underline{\text{Au}}$:Er sensors (cross pick-up between the thermometers) is minimized. In our current setup, this cross pick-up is in the range of 2 - 5 %. This small amount of cross pick-up only slightly changes the absolute value of the measured thermal conductivity, but has no pronounced effect on the qualitative temperature dependence, i.e., the exponent of the temperature. There is also an intrinsic reason for using a gradiometric arrangement. Consider a glass, like Duran, which has a relatively large magnetic moment. As temperature changes, it will exhibit a temperature-dependent magnetization that contributes to the total flux in the pick-up loop. However, this only results in a constant or linear flux distribution, such that the gradiometer is not sensitive to this change.

In order to avoid pick-up of stray flux from the environment, the Nb wires between the pick-up coils and the SQUID input loops are twisted pairwise, and shielded by superconducting PbSn tubes. To provide a small static magnetic field for the magnetization measurement, the setup is enclosed by an aluminum cylinder on which a superconducting coil is wrapped. Prior to the measurement, a static field B oriented along the sample's axis is frozen in by applying an appropriate current in the superconducting coil and heating the Al cylinder above its critical temperature T_{c}

for a short time. After cooling back down to $T < T_c$, the superconducting cylinder both maintains this field, and shields against external magnetic fields.

The static magnetic field used in our experiment has a magnitude of $B \simeq 5 - 10$ Gauss. In this field, the magnetization M of the Au:Er sensors used in our measurements deviates slightly from an ideal Curie behavior, which would yield $M(T) \propto 1/T$. This is not critical for the experiment's performance, since the thermometry method described here merely requires a sufficiently steep dependence of M on the temperature T.

To understand how the change in a sensor's magnetization M is reflected by the readout signal of the associated SQUID magnetometer, brief reviews of the SQUID circuitry and of the low temperature properties of Au:Er alloys will be presented in the following sections. The procedure of determining the temperature of the Au:Er sensors from the SQUIDs' output signals will be discussed in section 3.5.3.

3.4 SQUID Magnetometer

The term *magnetometer* here describes a device which consists of a magnetic flux transformer, and a flux-voltage converter. The transformer detects the flux changes occurring at its pick-up loop, for example due to magnetization changes of the paramagnetic sensors attached to the glass sample, and couples these changes into a dc SQUID. The latter then functions as a flux-voltage converter. These two components will now be described in more detail.

3.4.1 dc SQUID

The dc SQUID is an electronic device which facilitates a transformation of the amount of magnetic flux to a voltage signal.

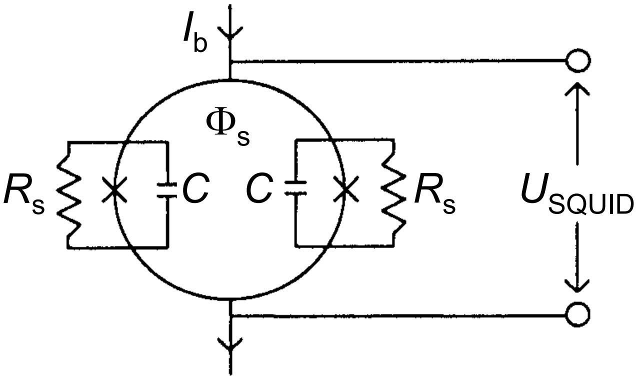

Fig. 3.7. Schematic diagram of a dc SQUID. The Josephson junctions are depicted by crosses. The capacities C are the intrinsic capacities of the Jopsephson junctions. The shunt resistors R_S suppress the hysteresis of the SQUID's current-voltage characteristics. (From Clarke (1996))

A dc SQUID, as shown in Fig. 3.7, is a superconducting loop which is interrupted by Josephson junctions at two points. These are thin insulating layers, which enable magnetic flux to enter the SQUID from the outside, and vice versa. Due to the quantum mechanical nature of the supercurrent, the voltage difference across the SQUID, U_{SQUID}, depends on both the bias current I_b, and on the magnetic flux Φ_s enclosed by the SQUID loop.

The current-voltage characteristics of a typical dc SQUID is shown on the left side of Fig. 3.8. If the bias current I_b is smaller than a certain critical current I_c, the current flowing through the SQUID is carried by superconducting Cooper pairs, which can tunnel through the thin insulating barrier; therefore, there is no voltage drop across the SQUID. This critical current depends on the geometry of the tunneling barriers, and also, in a periodic manner, on the magnetic flux Φ_s enclosed by the SQUID loop.

On the left side of the figure, two extreme cases of the current-voltage dependence are shown, which correspond to magnetic flux values of $\Phi_\mathrm{s} = n\,\Phi_0$, and $\Phi_\mathrm{s} = (n + 1/2)\,\Phi_0$, where $\Phi_0 = h/2e$ is the "flux quantum", and n is an integer. If the bias current I_b is chosen to be slightly greater than the maximum critical current, the voltage difference across the SQUID will depend greatly on the flux through the SQUID loop. From the right side of Fig. 3.8, it is apparent that the voltage U_SQUID depends on the flux Φ_s periodically. This pronounced dependence makes the SQUID useful as a flux-to-voltage converter.

The useful flux range for such a flux-voltage converter, within which the voltage across the SQUID is monotonically dependent on the magnetic flux through the SQUID loop, is limited to a narrow interval with a width of about $\Phi_0/2$. Hence, usually an additional electronic circuit is utilized to turn the SQUID into a linear component over a broad flux range. The circuit performing this task in the present experiment is the flux-locked loop circuit, which will be described in the next section.

3.4.2 Flux-Locked Loop Circuit

The combination of a dc SQUID and a flux-locked loop circuit forms a linear flux-voltage converter. In this case, the readout signal is no longer the voltage change across the SQUID. Instead, by means of a feedback system, the flux-locked loop circuit keeps the working point of the SQUID at

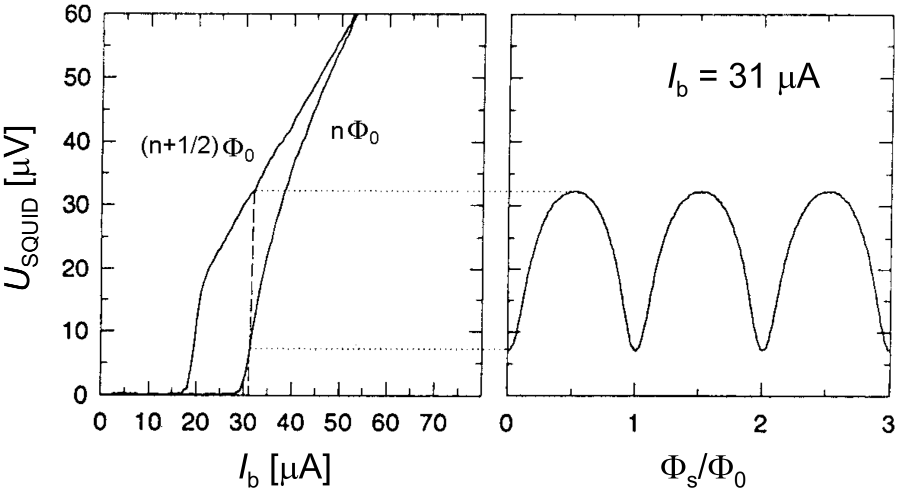

Fig. 3.8.
left: Current-voltage characteristics of a typical dc SQUID, with the two extreme cases $\Phi_\mathrm{s} = n\Phi_0$ and $\Phi_\mathrm{s} = (n + \frac{1}{2})\Phi_0$.
right: Flux-voltage characteristics for a fixed bias current $I_\mathrm{b} > I_\mathrm{c}$.
(Clarke 1996)

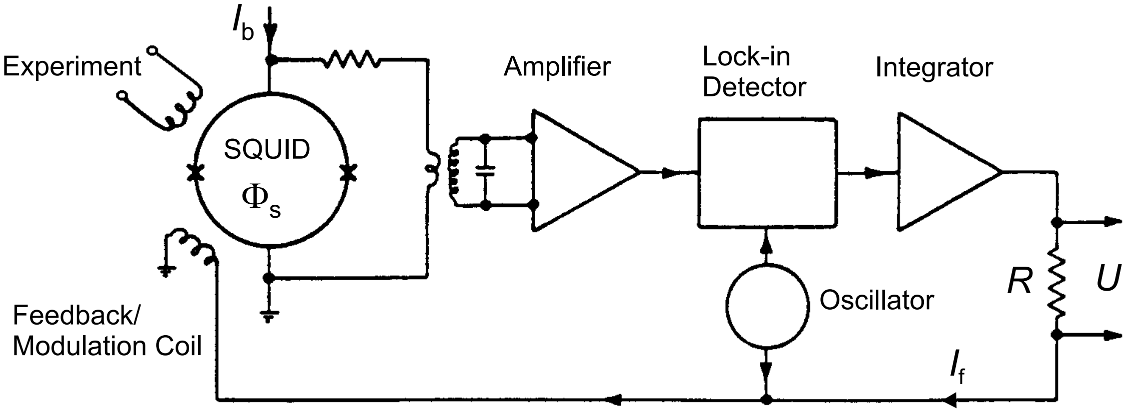

Fig. 3.9. Principle of a flux locked loop circuit. This circuit facilitates the use of a dc SQUID as a flux-voltage transformer with a linear characteristics. (From Clarke (1996))

one of the extrema of the flux-voltage characteristics, and uses the feedback current I_{f} to indicate the flux change.

As shown in Fig. 3.9, part of the voltage drop across the SQUID is used as the input signal of the regulation unit. If any change in this voltage is detected, an appropriate feedback current will be sent through the feedback coil to compensate the change in Φ_{S}. To improve the sensitivity of the voltage change measurement, the lock-in technique is applied, in which the feedback current is superposed by a modulation current. The resulting modulation of the voltage across the SQUID leads to a more sensitive differential signal used to regulate the current in the feedback loop.

The feedback current is proportional to the flux change in the SQUID loop and is read out by measuring the voltage U across a feedback resistance R, i.e., $\delta\Phi_{\mathrm{S}} \propto I_{\mathrm{f}} = U/R$. The conversion of the flux change in the experiment's pick-up coil to the flux change in the SQUID loop will be discussed in the next section.

The feedback and SQUID readout electronics used in the present experiment are part of the pcSQUID system[4], which has a bandwidth of approximately 100 kHz. The noise spectrum of this system is composed of mainly two contributions. The first is a "white noise" spectrum with a constant spectral density of about 4 $\mu\Phi_0/\sqrt{\mathrm{Hz}}$. At very low frequencies, this is superposed by a "$1/f$ noise" spectrum. At a frequency of 1 Hz, the contribution of $1/f$ noise is approximately ten times as great as that of the white noise.

3.4.3 Transfer Function of the Magnetometer

In the magnetometer discussed here, any change of magnetization δM in the sample is detected by the pick-up coil as a flux change $\delta\Phi_{\mathrm{p}}$, and coupled into the SQUID via the flux transformer. The arrangement used is sketched in Fig. 3.10.

In the following, we will derive how the measured voltage change δU reflects the flux change $\delta\Phi_{\mathrm{p}}$ detected by the pick-up coil.

At low temperatures, the flux transformer circuit is entirely superconducting. Hence, the magnitude of the magnetic flux through its enclosed area is constant, and is identical to the magnitude of

---

[4] pcSQUID PC-1000. STAR Cryoelectronics, Santa Fe, New Mexico.

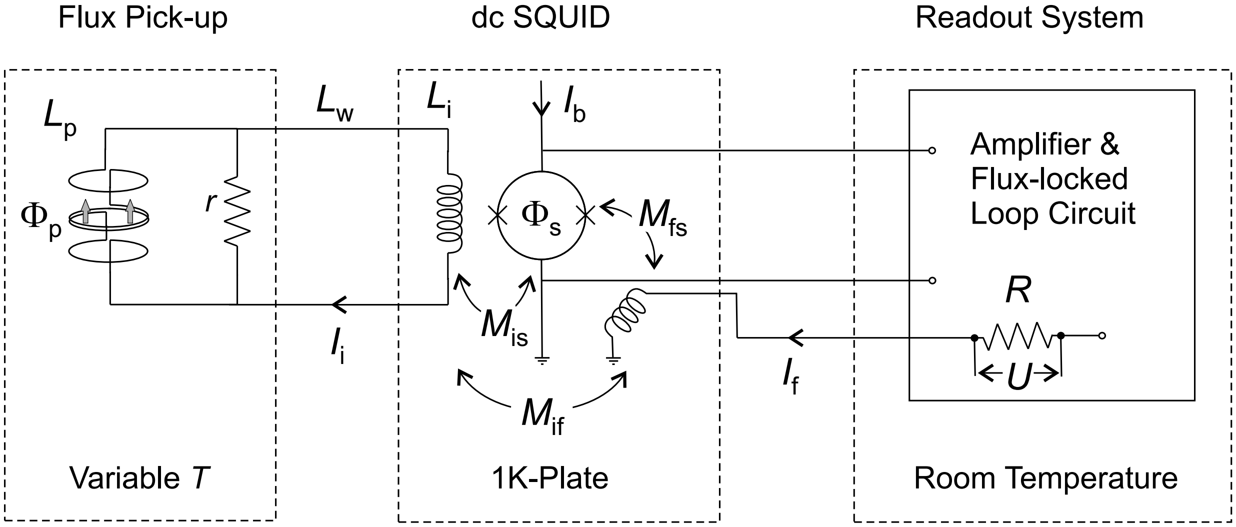

Fig. 3.10. Schematic of the magnetometer. Flux changes $\delta\Phi_\mathrm{p}$ detected by the pick-up coil are coupled into the SQUID via the flux transformer. The quantity measured is the voltage change δU in the feedback circuit.
The quantities indicated are:

Φ_p	Flux through pick-up coil	I_i	Current in SQUID input coil
Φ_s	Flux through SQUID loop	I_f	Feedback current
L_p	Inductance of pick-up coil	R	Resistance in feedback circuit
L_w	Inductance of wires	U	Output voltage
L_i	Inductance of SQUID input coil	r	Shunt resistor damping ac noise (see section 4.4)
$\mathcal{M}_\mathrm{xy}$	Mutual inductances		

magnetic flux that has been frozen in during cool-down. Any change in the magnetic flux through the pick-up coil, $\delta\Phi_\mathrm{p}$, will therefore be compensated by changes in the currents within the transformer and in the feedback circuit, δI_i and δI_f, respectively. The flux balance for the transformer loop can be written as

$$\delta\Phi_\mathrm{p} + (L_\mathrm{p} + L_\mathrm{w} + L_\mathrm{i})\delta I_\mathrm{i} + \mathcal{M}_\mathrm{if}\delta I_\mathrm{f} = 0\,. \tag{3.4}$$

The quantities used here are explained in the caption to Fig. 3.10.

The magnetic flux through the SQUID loop is governed by another relation, which contains contributions from both the input coil and the feedback circuit, and from the flux noise $\delta_\mathrm{n}\Phi_\mathrm{s}$ in the SQUID itself.[5] The noise contribution, however will be neglected here for simplicity. The net flux change in the SQUID loop reads

$$\delta\Phi_\mathrm{s}^\mathrm{net} = \delta I_\mathrm{i}\mathcal{M}_\mathrm{is} + \delta I_\mathrm{f}\mathcal{M}_\mathrm{fs}\,. \tag{3.5}$$

A characteristic quantity for the magnetometer is the specific voltage change $U_{\Phi_0} = R\,\delta I_{f,\Phi_0}$, which corresponds to the change in feedback current $\delta I_{f,\Phi_0}$ that causes a flux change in the SQUID of $\delta\Phi_\mathrm{s}^\mathrm{net} = \Phi_0$, where the latter designates the flux quantum $\Phi_0 = h/2e$. In the absence of the transformer (i.e., with an open input loop and $\delta I_\mathrm{i} = 0$), we find that

---

[5] The various contributions to the flux noise $\delta_\mathrm{n}\Phi_\mathrm{s}$, originating within the SQUID and in the associated electronics, are discussed in Clarke, Goubau, and Ketchen (1976).

$$U_{\Phi_0}^{\text{open}} = R\,\delta I_{f,\Phi_0} = R\frac{\Phi_0}{\mathcal{M}_{\text{fs}}}\,. \tag{3.6}$$

In the presence of the superconducting transformer loop, however, both conditions presented by equations (3.4) and (3.5) have to be met. The voltage change corresponding to a flux change Φ_0 in the SQUID loop is then given by

$$U_{\Phi_0} = U_{\Phi_0}^{\text{open}} \left\{ \frac{1}{1-\frac{\mathcal{M}_{\text{is}}\mathcal{M}_{\text{if}}}{\mathcal{M}_{\text{fs}}L_{\text{i}}}\,\frac{L_{\text{i}}}{L_{\text{p}}+L_{\text{w}}+L_{\text{i}}}} \right\}. \tag{3.7}$$

This value is greater than $U_{\Phi_0}^{\text{open}}$ in the case of an open input loop. This happens as the current I_{f} in the feedback coil causes a magnetic field which also induces a current I_{i} in the input coil, due to a mutual inductance $\mathcal{M}_{\text{if}} \neq 0$. The current I_{i} then in turn partially compensates the effect of the feedback current on the SQUID loop.

We shall return briefly to Eq. (3.5). As outlined in the previous section, the flux-locked loop technique is based on keeping the total flux Φ_{s} through the SQUID loop constant for a constant bias current I_{b}. Hence, during operation, it holds that

$$\delta\Phi_{\text{s}}^{\text{net}} = 0\,. \tag{3.8}$$

Combining this with the conditions set by equations (3.4) and (3.5), the voltage change δU resulting from a flux change $\delta\Phi_{\text{p}}$ in the pick-up loop can be determined, and it reads

$$\delta U = U_{\Phi_0}^{\text{open}}\,\frac{\delta\Phi_{\text{p}}}{\Phi_0}\left(\frac{\mathcal{M}_{\text{is}}}{L_{\text{p}}+L_{\text{w}}+L_{\text{i}}\left(1-\frac{\mathcal{M}_{\text{is}}\mathcal{M}_{\text{if}}}{\mathcal{M}_{\text{fs}}L_{\text{i}}}\right)}\right) = U_{\Phi_0}\,\frac{\mathcal{M}_{\text{is}}}{L_{\text{p}}+L_{\text{w}}+L_{\text{i}}}\,\frac{\delta\Phi_{\text{p}}}{\Phi_0}\,, \tag{3.9}$$

i.e., δU is linear in the flux change $\delta\Phi_{\text{p}}$.

$U_{\Phi_0}^{\text{open}}/R$	L_{i}	$\mathcal{M}_{\text{is}}$	$\dfrac{\mathcal{M}_{\text{is}}\mathcal{M}_{\text{if}}}{\mathcal{M}_{\text{fs}}L_{\text{i}}}$
5.5 μA	620 nH	10 nH	0.922

Table 3.1. Properties of the SQUIDs used in the experiment. The two SQUIDs are nearly identical.

A flux change $\delta\Phi_{\text{p}}$ in the pick-up coil can be caused by a magnetization change δM of the sensor situated within the coil. For a sensor volume V, and a pick-up coil with radius R_{p}, the flux change then turns out to be

$$\delta\Phi_{\text{p}} = \frac{G\,\mu_0}{R_{\text{p}}}\;V\,\delta M\,, \tag{3.10}$$

where G is a *geometry factor* reflecting the shapes of both the sensor and the pick-up coil. (The geometry of the pick-up coil will be discussed in more detail in the next section.)

This has the important implication that, if changes in the flux through the pick-up coil are only due to magnetization changes of the sensor, the voltage change δU in the feedback circuit is directly proportional to the magnetization change δM.

The role of the quantity U_{Φ_0} in the experiment should be mentioned. Whenever the flux-locked loop feedback circuit is employed, any flux change in the pick-up coil is associated with a change in the voltage U. However, the electronics of the feedback circuit operates only within certain voltage bounds, e.g., ±10 V. When these bounds are exceeded, the feedback circuit is temporarily disabled and the voltage U is set to zero. Since the flux-voltage characteristics is a periodic function of Φ, i.e., $U_{\mathrm{SQUID}}(\Phi) = U_{\mathrm{SQUID}}(\Phi + \Phi_0)$ (see Fig. 3.8), the circuit will then find the nearest operation point which has a flux difference of $n\,\Phi_0$ compared to the original one, with an integer n. We relate to this process as a "flux jump" performed by the circuit. In the feedback signal, this flux jump results in a "voltage jump" $\Delta U = n\,\Delta U_{\Phi_0}$. If the value of U_{Φ_0} is obtained experimentally, the integer n can be determined unambiguously, such that a continuous voltage signal can be reconstructed.

3.4.4 Pick-up Coils

The pick-up coils which we use to detect the magnetization of our paramagnetic sensors are second order gradiometers, wrapped with a superconductive niobium wire of 200 µm diameter. They are cast in a cylindrical support made of STYCAST 1266 epoxy, which is placed around the glass sample in such way that each coil is centered at its associated sensor. This arrangement is sensitive to flux distributions which have a maximum near the coil's center, but suppresses flux distributions which are constant, or have a linear gradient.

By using a finite element simulation software[6], it is possible to determine the signal size and cross pick-up for different coil and sensor arrangements. In Fig. 3.11, two different coil geometries are shown. In graph **(a)**, the pick-up coils consist of simple loops, whereas in graph **(b)**, they are second-order gradiometers, as used in our experimental setup.

As an example to demonstrate the difference between the two cases depicted in **(a)** and **(b)**, consider both arrangements to contain coils of diameter 5.3 mm, positioned around a glass sample of diameter 4 mm; the distance between the coils is $L = 3$ mm, and the sensors have a height of 1 mm, and a thickness of 0.2 mm. In the case of the gradiometer, the width between the windings is $\delta = 1$ mm.

Now, in each case the upper sensor (sensor #1) is assumed to have a certain finite magnetization, while the magnetization of the lower sensor (sensor #2) is zero. Let Φ_1^{simple} and Φ_2^{simple} denote the total flux generated by sensor #1 in the upper and lower coil of the simple loop arrangement, respectively. The corresponding quantities for the gradiometer are Φ_1^{grad} and Φ_2^{grad}.

For the amplitudes of the signals in the upper coils, we find the ratio $\Phi_1^{\mathrm{simple}}/\Phi_1^{\mathrm{grad}} = 1.69$, i.e., using a gradiometric pick-up coil leads to a loss in signal amplitude of about 40 %. However, this loss is amended in regard to the measure of cross pick-up, i.e., stray flux from sensor #1 picked up by the coils associated with sensor #2. For the simple loop, we find a "cross pick-

---

[6] FEMM. Developed by D. Meeker.

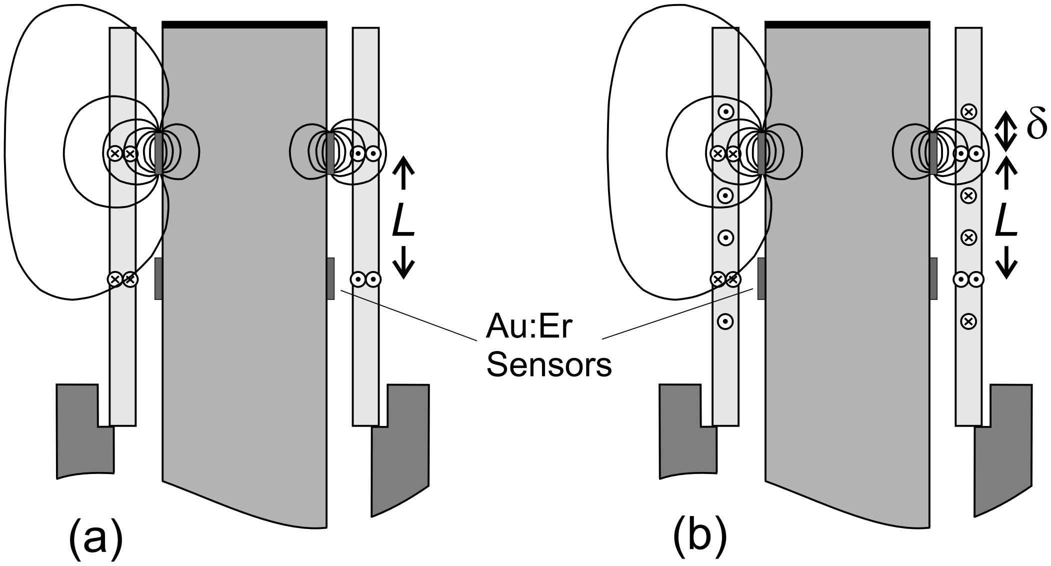

Fig. 3.11. Pick-up coils consisting of simple loops **(a)**, and second-order gradiometers **(b)** as used in this experiment. The magnetic flux lines have been calculated using a finite element simulation.

up factor" of $\gamma^{\text{simple}} = \varPhi_2^{\text{simple}}/\varPhi_1^{\text{simple}} = 8.3\,\%$, whereas for the gradiometer, this quantity is $\gamma^{\text{grad}} = \varPhi_2^{\text{grad}}/\varPhi_1^{\text{grad}} = 3.5\,\%$. Identical results will be found if we exchange the roles of the sensors #1 and #2 in the calculation. Hence, cross pick-up between the two coils can be described by a single mutual "cross pick-up factor" γ.

For the gradiometers used in our experiments, we determined cross pick-up to be on the order of $\gamma \simeq 1\text{-}4\,\%$. A correction for this effect can be applied to the measurement signal in the following manner.

Consider two coils with mutual cross pick-up of magnitude γ. The two paramagnetic sensors in general have different amounts of magnetization, due to their different temperatures. The total amount of flux enclosed by either one of the two coils, $\varPhi_i$ $(i = 1, 2)$, has a contribution from its corresponding sensor, denoted as $\varPhi_i^0$, and and a cross pick-up contribution from the non-corresponding sensor, $-\gamma\,\varPhi_j^0$ $(j \neq i)$. Hence, the relationship between the net flux pick-up $(\varPhi_1, \varPhi_2)$ and the sole contribution from the corresponding sensors, $(\varPhi_1^0, \varPhi_2^0)$, can be written as

$$\begin{pmatrix} \varPhi_1 \\ \varPhi_2 \end{pmatrix} = \begin{pmatrix} 1 & -\gamma \\ -\gamma & 1 \end{pmatrix} \begin{pmatrix} \varPhi_1^0 \\ \varPhi_2^0 \end{pmatrix}. \tag{3.11}$$

From this, we find the desired correction formula as

$$\begin{pmatrix} \varPhi_1^0 \\ \varPhi_2^0 \end{pmatrix} = \frac{1}{1-\gamma^2} \begin{pmatrix} 1 & \gamma \\ \gamma & 1 \end{pmatrix} \begin{pmatrix} \varPhi_1 \\ \varPhi_2 \end{pmatrix}. \tag{3.12}$$

In the evaluation of the data acquired in our experiment (see section 3.5.3), we found that the reduction in the signals due to cross pick-up does not noticeably influence our results for the thermal conductivity. However, for a similar setup using pick-up coils consisting of simple loops, this correction would probably be necessary.

3.4.5 Paramagnetic Sensor Material

For a paramagnetic material, the magnetization M and magnetic susceptibility χ, at temperature T and in a magnetic field of strength B, can be expressed as

$$M(T) = \frac{\chi(T)}{\mu_0} B = NgJ\,\mu_B B_J(h)\,, \quad \text{with } h = \frac{gJ\,\mu_B B}{k_B T}\,, \tag{3.13}$$

where μ_0 is the permeability of free space, N the number of paramagnetic atoms, g the Landé factor, J the total angular momentum of each paramagnetic atom, μ_B the Bohr magneton, and B_J the Brillouin function defined as

$$B_J(h) = \frac{2J+1}{2J} \coth\left[\frac{(2J+1)h}{2J}\right] - \frac{1}{2J}\coth\left(\frac{h}{2J}\right). \tag{3.14}$$

For very low temperatures, or high fields, it holds that $h \gg 1$, and the magnetization and susceptibility become constant. However, for $h \ll 1$, i.e., if the thermal energy $k_B T$ is high compared with the energy splitting $gJ\,\mu_B B$ due to the magnetic field, Eq. (3.13) reduces to the Curie law

$$M(T) = \frac{\chi(T)}{\mu_0} B = \frac{\lambda_C}{\mu_0}\frac{B}{T}\,, \tag{3.15}$$

where $\lambda_C = NJ(J+1)\,\mu_0\mu_B^2 g^2/3k_B$ is the Curie constant. Hence, for temperature and magnetic fields that result in $h \ll 1$, such a paramagnetic material can be used as a thermometer.

The paramagnetic sensors used in our experimental setup are made from a dilute alloy of erbium in gold (<u>Au</u>:Er), where erbium in its natural isotopic composition has been used (see Table 3.2). The sensors were cut from a piece of <u>Au</u>:Er whose erbium concentration has been determined as approximately 480 ppm by Fleischmann (1998).

Binary alloys of erbium in gold have been reviewed comprehensively by Fleischmann et al. (2000) and Enss et al. (2000) , so that only a few key facts will be mentioned here. At temperatures below 1 K, and in weak magnetic fields, the dopant Er^{3+} ions can occupy only the two states with

Isotope	Nuclear Spin	Proportion
^{162}Er	0	0.14 %
^{164}Er	0	1.61 %
^{166}Er	0	33.6 %
^{167}Er	7/2	22.95 %
^{168}Er	0	28.8 %
^{170}Er	0	14.9 %

Table 3.2. Natural isotopic composition of the rare earth erbium. (From CRC Handbook of Chemistry and Physics, 76th Edition, 1996.)

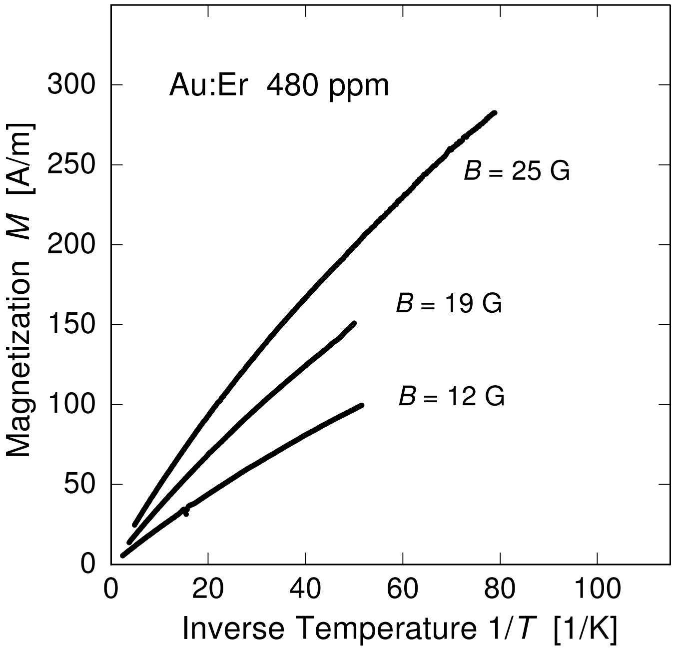

Fig. 3.12. Measured magnetization of a Au:Er 480 ppm sample in different magnetic fields. (From Fleischmann et al. (2000))

the lowest energy, called the "Γ_7-Kramers doublet" (Williams and Hirst 1969). Hence, the ions can be regarded as two-level systems, with an quasi-spin $\tilde{S} = 1/2$, and an effective isotropic Landé factor $\tilde{g} = 6.8$ (Tao, Davidov, Orbach, and Chock 1971).

With these values, and for a typical field strength $B \simeq 10$ Gauss and temperature $T \simeq 20$ mK, the parameter h from Eq. (3.13) evaluates to $h \simeq 0.12$, suggesting that above 20 mK, the magnetization should behave according to the Curie law in Eq. (3.15). However, deviations from the Curie law occur at much higher temperatures, due to a hyperfine splitting caused by the non-zero nuclear spin of the ^{167}Er isotope, and the interactions between the dopant erbium ions. This has been discussed in detail by Fleischmann et al. (2000). Figure 3.12 shows the temperature dependence for the magnetization of Au:Er 480 ppm for several field strengths. Compared to the

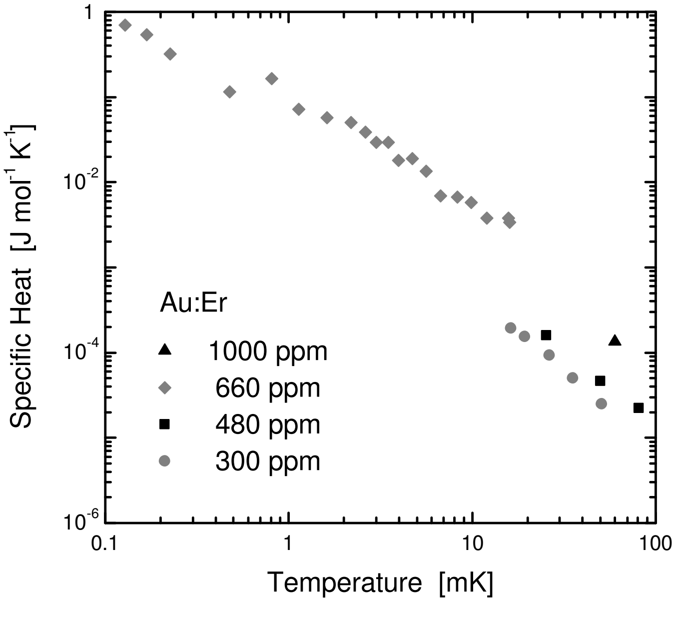

Fig. 3.13. Specific heat of Au:Er alloys with different erbium concentration. The data on the 660 ppm magnetic sample are from Herrmannsdörfer et al. (2000), the data on all other samples are from Enss et al. (2000).

behavior predicted by the Curie law, a flattening of the magnetization is visible at relatively high temperatures already.

However, this does not affect our use of <u>Au</u>:Er alloys as sensor materials, as we do not use the sensors as primary thermometers. Rather, we generate a magnetization-to-temperature calibration table for each measurement, such that we do not rely on a specific characteristics of the magnetization $M(T)$ of <u>Au</u>:Er. The only requirement is that the slope $\partial M/\partial T$ is steep enough, i.e., that a variation in temperature results in a large change in magnetization, to allow for a high sensitivity.

Another property of <u>Au</u>:Er which is of great importance for the performance of our measurement is the alloy's heat capacity. It has been found by Herrmannsdörfer, König, and Enss (2000) that, at temperatures below 10 mK, the specific heat C_{AuEr} of <u>Au</u>:Er 660 ppm is roughly proportional to $T^{-1.1}$. Hence, in a thermal conductivity measurement with our experimental setup, the heat capacity of the paramagnetic sensors, C_{AuEr}, increases at lower temperatures, as shown in Fig. 3.13, while the heat capacity of the glass sample, C_{glass}, decreases roughly linear with decreasing temperature, as it has been found in numerous experiments by other investigators (see section 2.1.1). As a consequence, at low temperature, the relaxation time of the system will be determined mainly by the paramagnetic sensors' large heat capacity.

3.5 Data Acquisition

3.5.1 Experimental Electronics

Figure 3.14 shows the electronic setup which is used for signal processing and data recording in this experiment. It consists of two dc SQUIDs with flux-locked loop feedback electronics and low-noise amplifier, additional low-pass filters, analog-digital (A/D) converters, and a computer which reads and stores the digitized signals.

The dc SQUIDs and the associated electronics are part of the commercially available pcSQUID system[7]. The SQUID controller contains a low-pass filter which, in our case, is set to 3 kHz on either SQUID channel. In order to suppress 50 Hz noise due to ac power supply, an additional RC low-pass filter with a cut-off frequency around 16 Hz is used on each channel. The resulting signals are digitized using A/D converters[8], and recorded by a computer at a sampling rate of about 100 Hz.

Both the A/D converters and the data acquisition computer are equipped with opto-electrical converters[9], such that the signal transmission is accomplished via optical fibers. Such an arrangement is advisable, since the cryostat and the A/D converters share a common electrical ground, and ground currents from the computer should be avoided, as they will lead to heating of the cryostat.

As mentioned above, the LED used to heat the glass sample is driven with a periodic square-wave signal of constant duration (~ 40 µs) and amplitude (~ 4 V). To generate this signal, several

---

[7] STAR Cryoelectronics, Santa Fe, New Mexico. Formerly distributed by Conductus Inc., Sunnyvale, California.

[8] Multiplexer A295D 12 Bit, ADC A295C 16 Bit. Developed by A. Rausch, Physical Institute, University of Heidelberg.

[9] Optical Fiber Interface A295A. Developed by A. Rausch.

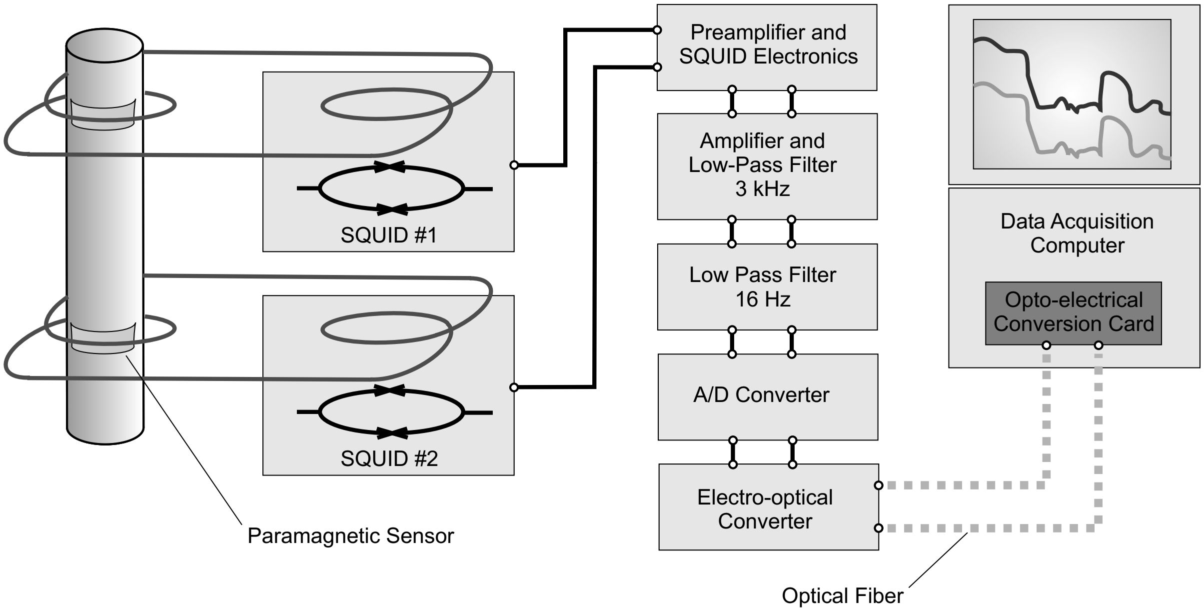

Fig. 3.14. Electronic setup of the SQUID magnetometer.

wave-form generators[10] can be used, all of which have a very high stability in both signal amplitude and timing. They facilitate signal repetition rates ν_{rep} between 0.1 Hz and 10 kHz, which allows for a heat input onto the sample, $\dot{Q}$, which can be varied over five orders of magnitude. The electric wires between signal generator and LED are floating with regard to the electrical ground of the cryostat, so that no ground current occurs.

The data acquisition procedure is carried out by an automated computer software developed in the programming language LabView[11], which controls the timing of the experiment, sets variable parameters, such as the mixing chamber temperature T_{MC} and the repetition rate ν_{rep} of the light pulses driving the LED, displays all relevant data, and stores the measurement signal on a hard-drive.

3.5.2 Measurement Procedure

Prior to a measurement, a small static magnetic field $B \simeq 5 - 10$ G is frozen in the aluminum field cylinder, as described in section 3.3.2. For the two magnetometers, the bias current of the SQUIDs, and the modulation current and phase of the associated flux-locked loop circuits have to be adjusted so that the voltages across the SQUIDs have the maximum sensitivity to flux changes.

Figure 3.15 shows the experimental routine of our thermal conductivity measurement. In graph **(c)**, the temperature in the mixing chamber is plotted versus time, while graph **(b)** shows the repetition rate of the periodic voltage signal applied to the LED, which is a direct measure for the heat input onto the sample, as described in section 3.3.2. A repetition rate of zero indicates that the LED is switched off. As seen from graph **(a)**, changes in the flux picked up from one of the paramagnetic sensors attached to the sample are correlated with the temperature of the mixing chamber, as well as with the heat input due to the LED. In the data set shown here, a

---

[10] DS340, DS345, DG535. Stanford Research Systems, Sunnyvale, California.

[11] LabView. National Instruments Corp., Austin, Texas.

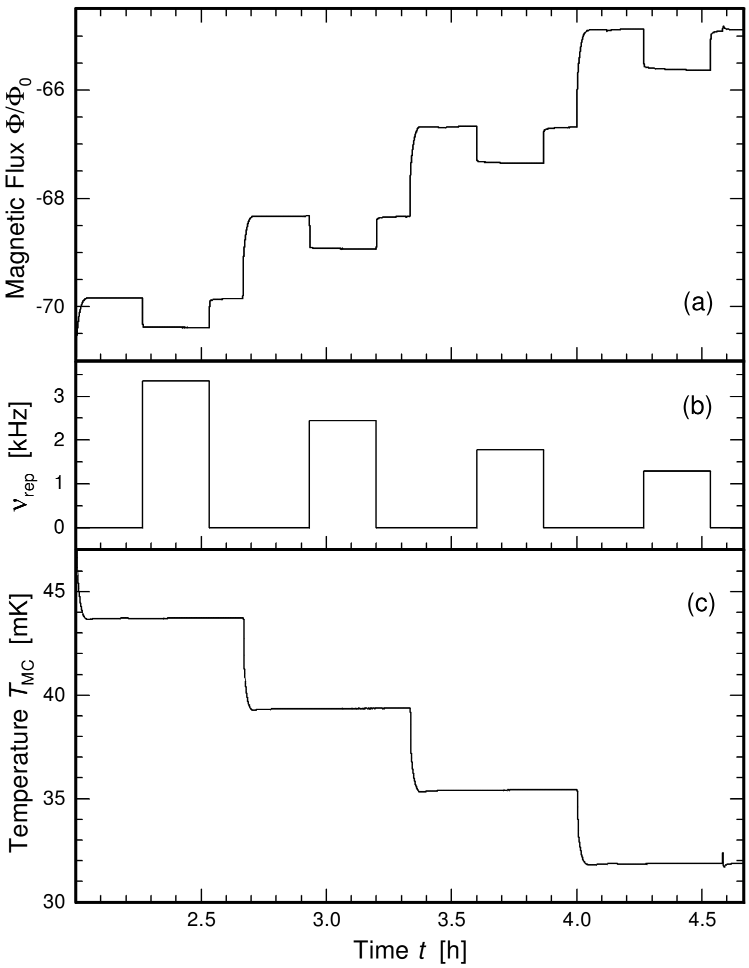

Fig. 3.15. Dependence of the magnetic flux generated by a paramagnetic sensor attached to the sample **(a)** on the heat input **(b)** and the mixing chamber temperature **(c)**.

rising flux signal indicates a decrease in temperature. (Whether the flux signal declines or rises with temperature depends on the polarity of the B field frozen in the aluminum cylinder, and is of no further significance for the measurement.)

It should be noted that the quantity actually recorded in the experiment to reflect the sensor's magnetization is the voltage read from the SQUID electronics. However, in the figure, this voltage has already been converted into a flux value for clarity. The procedure for this conversion will be explained in section 3.5.3.

As seen in the figure, the thermal conductivity measurement is performed for a series of fixed mixing chamber temperatures T_{MC}, with a difference of about 10 % of the absolute temperature between two successive steps. In each temperature step, after the glass sample has entirely thermalized, i.e., the voltage signal reading from the SQUID electronics is constant in time, the LED is switched on to generate a power dissipation of $\dot{Q} \propto \nu_{\mathrm{rep}}$ in the glass. Here, a thermal gradient develops within the sample, until a steady state is reached. After that, the LED is switched off, and the sample thermalizes back to T_{MC}.

When choosing the repetition rate ν_{rep}, in order to minimize statistical errors in the evaluation of the thermal conductivity, a marked increase of about 10 % in the sensor's temperature upon turning on the LED is desirable, e.g., $\varrho \equiv (T_1 - T_{\mathrm{MC}})/T_{\mathrm{MC}} = 10\,\%$, where T_1 is the steady state temperature of the sensor while the LED is on. This relative temperature change can be kept approximately constant over the entire temperature range of the experiment by regulating the repetition rate such that $\nu_{\mathrm{rep}} \propto T^3$. This is understood as $\dot{Q} \propto \nu_{\mathrm{rep}} \propto \kappa\, \mathit{\Delta} T$, with the assumption that $\kappa \propto T^2$ over most of the measuring temperature range.

In section 4.2, we will demonstrate that, as long as the relative temperature change is small, e.g., $\varrho \lesssim 10\,\%$, our results do not depend on the magnitude of ϱ, hence it does not need to be kept constant.

Note that the absolute amount of power $\dot{Q}$ dissipated at the glass sample is not known. It holds that $\dot{Q}/\nu_{\mathrm{rep}}$ is constant, but the absolute value of this expression cannot be easily determined. The coupling between LED and optical fiber is unknown, so is the throughput of the fiber, and the proportion of light reflected by the absorber film on top of the glass sample. This issue must be addressed when attempting to determine absolute thermal conductivity values from the acquired data (see discussion in section 3.5.3).

In the temperature range above 25 mK, as in the data set shown in Fig. 3.15, the system's relaxation time τ is in the range of a few minutes, so that measurements at these temperatures can be performed relatively fast. However, τ increases rapidly towards lower temperatures, such that the time allowed for the system to thermalize has to be increased. Consider a very good thermal boundary conductance between the glass sample and its copper holder, such that the relaxation time is $\tau \propto C/\kappa$. Here, κ is the thermal conductivity of the glass, which follows roughly $\kappa \propto T^2$ in the temperature range of interest. The heat capacity of the system is composed of two parts, $C = C_{\mathrm{glass}} + C_{\mathrm{AuEr}}$. Within our system, C_{AuEr} is much larger than C_{glass}, and with a small magnetic field it depends only weakly on temperature between 10 mK and 100 mK; hence in this range it holds roughly that $\tau \propto 1/T^2$. Below 10 mK, the heat capacity C_{AuEr} increases rapidly due to spin-spin interactions, which results in a steeper increase in τ below that temperature.

Due to this temperature-dependent thermal relaxation time, the measuring time t_{tot} for each temperature step T is chosen to scale according to the relation $t_{\mathrm{tot}} \propto 1/T^2$, with a sufficiently long interval $t_{\mathrm{tot}}(5\ \mathrm{mK})$.

3.5.3 Data Evaluation Procedure

In this section, we will describe the evaluation procedure, with which we derive the thermal conductivity of the glass sample from the acquired data. We will use the data acquired from a vitreous silica sample as an example to illustrate the data evaluation process. This sample had the geometry of a hollow cylinder, with an outer diameter of 4 mm and an inner diameter of 2 mm.

In the following description, the time-dependence of the variable quantities is suppressed, e.g., instead of $U_1(t)$ and $\mathit{\Phi}_1(t)$, we write U_1 and $\mathit{\Phi}_1$, whenever no ambiguities arise from doing so.

In the first processing step, the voltage signals read from the SQUID feedback electronics associated with the two magnetometers, U_1 and U_2, are transformed into the corresponding amounts of magnetic flux in the SQUID loops, $\mathit{\Phi}_1$ and $\mathit{\Phi}_2$, in units of the "flux quantum" $\mathit{\Phi}_0 = h/2\,e$ (see section 3.4.3). Any discontinuities in the signals, due to "flux jumps" of $n\,\mathit{\Phi}_0$ performed by the feedback circuit, are then removed by using an interactive computer program which reconstructs a continuous flux curve.

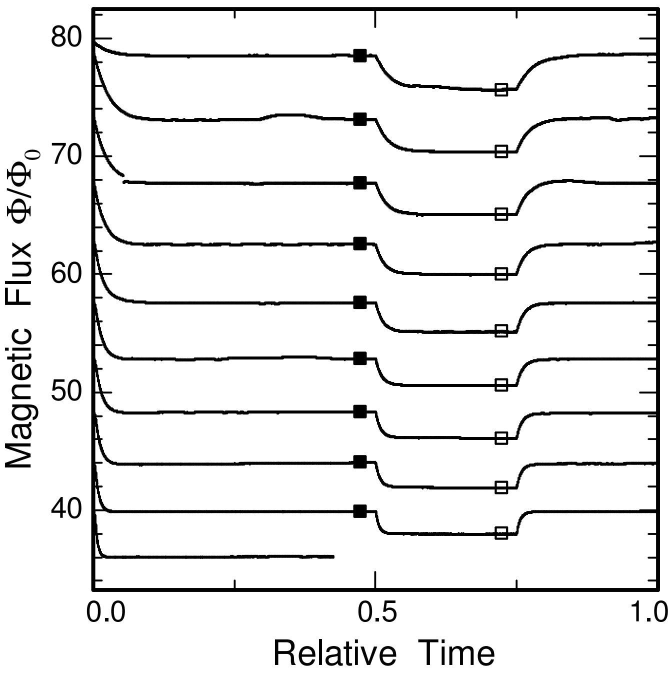

Fig. 3.16. Magnetic flux readings, obtained from one of the two paramagnetic Au:Er sensors attached to a vitreous silica sample. This data set covers the temperature range between 6 mK and approximately 14 mK. Full marks (■) indicate points that are used to generate a flux-temperature conversion table. Empty marks (□) indicate data which have been used to determine the steady-state temperature of the sensor while a constant heat input is applied by means of the LED.

Figure 3.16 shows the reconstructed continuous flux curve read by one of the SQUID thermometers. To make the comparison between data taken at different temperatures easier, the elapsed time t at each temperature is normalized in regard to the duration t_{tot} of the temperature step in the evaluation procedure, and we term the resulting parameter t/t_{tot} as "relative time". The graph covers the temperature range between 6 mK (upper part) and about 14 mK (lower part). Here, an increase of the sensor's temperature results in a decrease of the magnetic flux in the SQUID loop.[12]

In order to obtain the absolute temperature of the paramagnetic sensors, a calibration table for each sensor is needed to perform the flux-to-temperature conversion. To generate a calibration table, using Fig. 3.16 as an example, one first determines the flux values marked in full, which indicate the time at each temperature step when the glass sample is thermalized and in equilibrium with the cryostat's mixing chamber, i.e., $T_{\mathrm{sensor}} = T_{\mathrm{MC}}$. From this, we obtain a set of "calibration points" (Φ, T) for each sensor, and by performing a cubic spline fit through these points, a continuous flux-temperature conversion curve can be realized.

After taking the calibration points, we turn to the data acquired when the LED was switched on to generate a constant heat input onto the sample. Now the empty marks are set at those values of the magnetic flux which represent the temperature of the sensor when a steady state is reached while heating. In these instances, a thermal gradient is present in the sample, and we can use the flux-temperature conversion functions that we have obtained earlier to determine the current temperature of the sensors.

Note that when extracting the values of magnetic flux or temperature from the marked points in the acquired data sets, these values are deduced by taking averages over significant time intervals, typically several minutes, in order to reduce statistical noise.

---

[12] If a correction for cross pick-up between the thermometers is desired, it is performed at this stage of the evaluation. See section 3.4.4 for details.

Figure 3.17 displays the flux-temperature calibration curve generated from the data set shown in the previous figure (points at higher temperatures were neglected in the earlier plot for simplicity). Here an offset has been removed, so that when $1/T \to 0$, it holds that $\Phi/\Phi_0 \to 0$, as stated by the Curie law. By plotting the curve in the representation of inverse temperature versus magnetic flux, the Curie-like behavior of the paramagnetic sensor's magnetization is emphasized. It is apparent that at temperatures below approximately 20 mK, an onset of saturation becomes visible in the $\underline{\text{Au}}$:Er sensor.

After transforming the magnetic flux curves for both paramagnetic sensors, temperature curves as shown in Fig. 3.18 are obtained. The lowest of the three curves represents the temperature in the cryostat's mixing chamber, T_{MC}. It appears that T_{MC} remains constant at each temperature step, apart from minor disturbances due to external influences, and that any heat input from the LED does not affect the temperature in the mixing chamber. The two upper curves represent the temperatures of the two paramagnetic sensors, which rise when the LED is switched on.

In the figure, some interesting details can be pointed out. First, in the $\log(T)$ representation, it appears that the relative rise in the sensors' temperature upon switching on the LED, $(T_{\mathrm{i}} - T_{\mathrm{MC}})/T_{\mathrm{MC}}$, with $i = \{1, 2\}$, is approximately constant over the temperature range shown, as it was intended by using a heat input $\dot{Q} \propto T^3$ (see section 3.5.2). Moreover, from the cooling rate of the temperature curves after the LED heating has been switched off, one can observe the system's thermal relaxation time τ. Here an increase in τ on the relative time scale becomes visible towards lower temperatures. With the duration of each temperature step scaled as $t_{\mathrm{tot}} \propto 1/T^2$, it is seen that τ scales with $T^{-\eta}$, $\eta > 2$ at lower temperatures, as discussed in section 3.5.2.

According to Eq. (3.2), the thermal conductivity of a sample can be determined if the power $\dot{Q}$ dissipated at the top of the sample, and two temperatures T_1 and T_2 along the temperature gradient are known. For a suitable medium temperature T_{mean}, the thermal conductivity reads

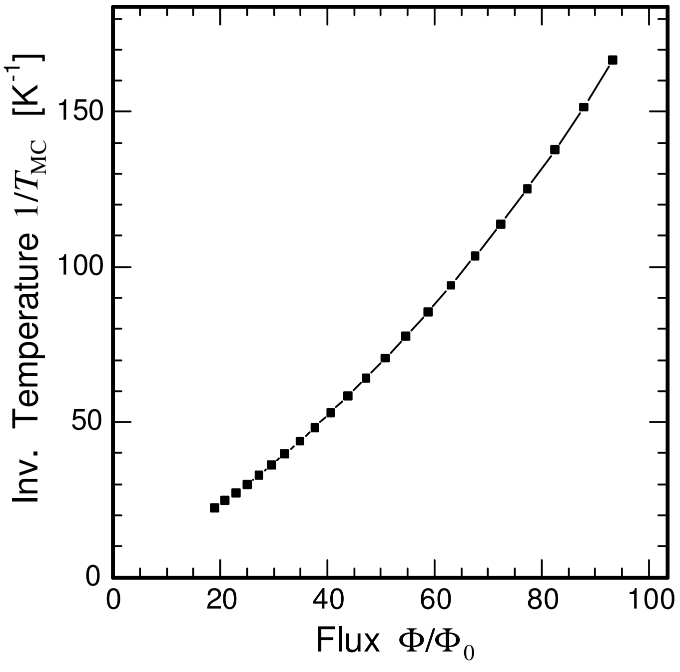

Fig. 3.17. Calibration curve for the transformation of magnetic flux Φ to absolute temperature T. This curve is derived from the data set displayed in Fig. 3.16.

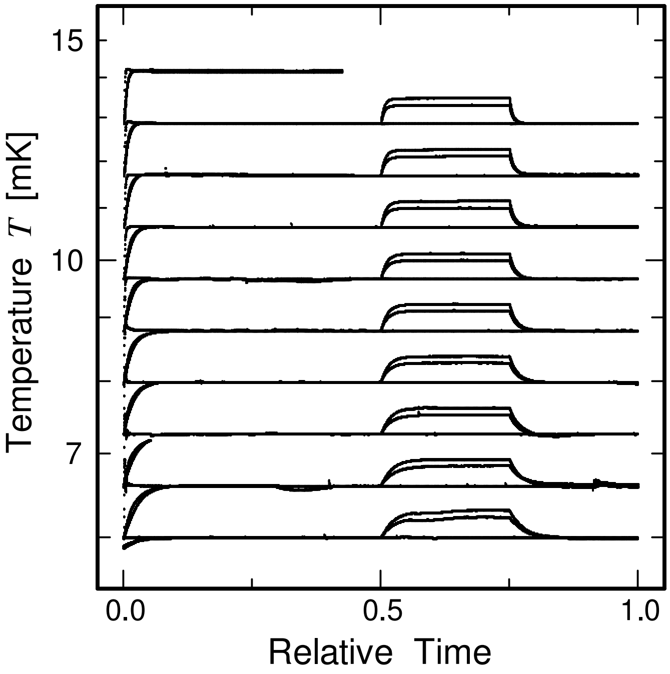

Fig. 3.18. Temperature of the cryostat's mixing chamber (bottom curve), and of the two paramagnetic sensors attached to the glass sample (top and middle curves). This graph refers to the same data set as used in Fig. 3.16 and Fig. 3.17.

$$\kappa(T_{\text{mean}}) = \frac{\dot{Q}}{A}\,\frac{L}{T_1 - T_2}\,, \tag{3.16}$$

where A and L denote the cross-section of the sample and the distance between the two thermometers, respectively. A convenient choice for the medium temperature is $T_{\text{mean}} = (T_1 + T_2)/2$.

It holds that the heat input into the sample is proportional to the repetition rate of the signal that drives the LED, i.e., $\dot{Q} \propto \nu_{\text{rep}}$. However, the absolute value of the heat input $\dot{Q}$ is not known. Hence, it is convenient to rewrite Eq. (3.16) as

$$\kappa(T_{\text{mean}}) = \alpha\,\frac{\nu_{\text{rep}}}{\Delta T}\,, \qquad \text{with} \quad \alpha = \frac{\dot{Q}}{\nu_{\text{rep}}}\,\frac{L}{A}\,, \tag{3.17}$$

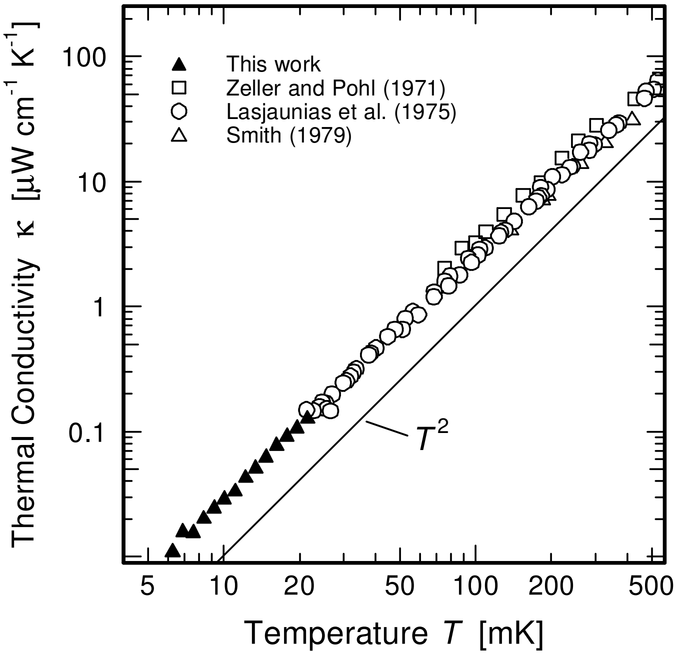

Fig. 3.19. The absolute value of our thermal conductivity data is adjusted to results from the literature. The T^2 curve has been added for comparison.

where $\Delta T = T_1 - T_2$, and all non-varying parameters are absorbed in a constant prefactor α. With the values ΔT and ν_{rep} from the measurement, we can use Eq. (3.17) to obtain the temperature dependence of the thermal conductivity of the glass sample. However, the absolute value of κ cannot be determined from the experimental data alone.

Absolute values for the sample's thermal conductivity are obtained by comparing the experimental data to the thermal conductivity data of similar substances found in the literature. This is done by adjusting the prefactor α in Eq. (3.17) so that, in a plot of $\log(\kappa)$ versus $\log(T)$, the literature values and the data taken from our measurement coincide in the temperature range of overlap, as shown in Fig. 3.19 for the same data set that was used in the previous graphs.

3.6 Glass Samples

The thermal conductivity measurements presented in this work have been performed on samples made of vitreous silica, F-320, and BK7.

Vitreous silica (silica glass, a-SiO_2) is a general term for natural and synthetic glasses which are composed almost exclusively of silicon dioxide ($> 99\,\%$). The vitreous silica sample used in our measurement has been supplied by the glass workshop of the Physical Institute, University of Heidelberg. It has been cut from a drawn bar of hollow cylindrical shape, with an outer diameter of 4 mm and an inner diameter of 2 mm, and it features a smooth surface. Information regarding the manufacturer or the exact chemical specification is not available.

F-320 is a synthetic silica glass, doped with a small amount of fluorine ($< 1\,\%$). It has an OH content of < 1 ppm, and a structure of fine layers.[13] F-320 is manufactured by Heraeus Quarzglas GmbH, Hanau. The sample used in our measurement has a diameter of 6 mm, and has a slightly roughened surface.

The borosilicate glass BK7 is produced by Schott Glaswerke, Mainz. The specifications of BK7 supplied by the manufacturer[14] give approximate ranges for the proportions of its chemical constituents. Apart from the main ingredient SiO_2 (60 - 70 %), in contains certain amounts of B_2O_3 (10 - 20 %), BaO ($<$ 1 - 10 %), Na_2O (1 - 15 %), and K_2O (5 - 15 %). Trace minerals with proportions below 1 % include ZnO, CaO, TiO_2, and Al_2O_3. The source of our BK7 sample is Hellma Optik GmbH, Jena. It has a diameter of 6 mm, and a roughened surface.

The BK7 and F-320 samples have been kindly provided to us by Dr. P. Strehlow, PTB Berlin.

Further specifications regarding the sample preparation, as well as the measurement parameters, are given in Table 4.1.

---

[13] Private communication from Heraeus Quarzglas GmbH, Hanau.

[14] Private communication from Schott Glaswerke, Mainz.

4. Results and Discussion

In this section, we present the results of the thermal conductivity measurements performed with our experimental setup. We will examine the reliability of our measuring procedure and our thermometers, and estimate the accuracy of our results. Besides, we will present a simulation that calculates the temperature distribution in our current experimental arrangement. Through this simulation, the thermal boundary (Kapitza) resistance between the glass samples and their copper holders can be estimated from the experimental data.

4.1 Measurement Results

The properties of the samples used in our measurements are listed in Table 4.1, which also specifies the geometries of the paramagnetic sensors and the pick-up coils, and the relevant measurement parameters. The results for the thermal conductivity have been obtained with the data evaluation procedure described earlier.

Note that in the evaluation of our data, for the ground temperature T_{MC} of each step, we have consistently used the temperature read from the carbon resistance thermometer described in section 3.2.2. The paramagnetic susceptibility thermometer (see section 3.2.3) has been used only for the cryostat's temperature regulation.

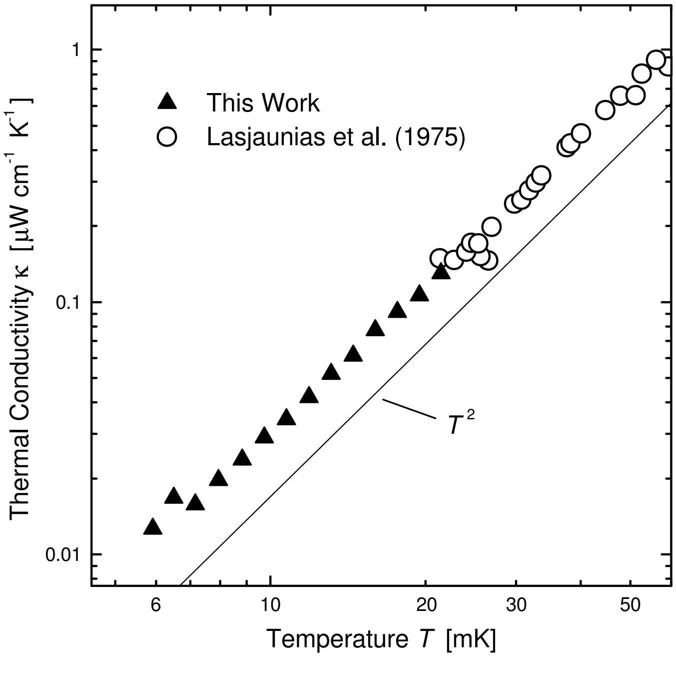

Fig. 4.1. Thermal conductivity κ of vitreous silica (sample #1). The T^2 curve has been added for comparison.

	Vitreous Silica (#1)	F-320 (#2)	BK7 (#3)
Shape	Cylindrical, Hollow	Cylindrical, Massive	Cylindrical, Massive
Dimension	Outer ∅ 4 mm Inner ∅ 2 mm Length 15 mm	∅ 6 mm Length 24.5 mm	∅ 6 mm Length 30 mm
Light Absorber	Al Tape (80 µm)	CuO Film (700-800 nm)	STYCAST 2850 ($\sim$ 1 mm)
L	3 mm	6 mm	6 mm
R_p / w	5.3 mm / 1 mm	6.8 mm / 2 mm	7.1 mm / 1.5 mm
γ	3.5 %	0.9 %	1.5 %
Magnetic Field Strength	9.7 G	3.8 G	5 G
Temperature range	6 - 21 mK	5.3 - 63 mK	7 - 46 mK

Table 4.1. Specifications of the samples and corresponding setups used in our thermal conductivity measurements. The quantity L describes the distance between the sensors; the parameters of a pick-up coils are its radius R_p and the width between the windings, w. The quantity γ describes the amount of cross pick-up between the two magnetometers, as described in section 3.4.4.

The thermal conductivity of vitreous silica (sample #1) is shown in Fig. 4.1, along with the literature data that are used to obtain an absolute value of our result. When performing a fit to a power law of the form $\kappa \propto T^\beta$, our data are best described by $\beta = 1.90 \pm 0.10$.

Having obtained an absolute value of the thermal conductivity, we can determine the power that has been dissipated on the sample to generate the temperature gradient. From Eq. (3.16), we find that

$$\dot{Q} = \kappa(T_\mathrm{mean})\,\frac{A}{L}\,(T_1 - T_2)\,, \tag{4.1}$$

where A and L denote the cross section of the sample and the distance between the two thermometers, respectively; the quantities T_1 and T_2 are the temperatures of the two paramagnetic sensors, and $T_\mathrm{mean} = (T_1 + T_2)/2$.

The heat input calculated for the measurement on sample #1 in this manner is shown in Fig. 4.2, for an extract of the data set which contains the data acquired at the lowest temperatures. The curves in the figure represent the mixing chamber temperature (gray curve), and the temperatures of the two sensors attached to the sample.

With typical amounts of intended heat input on the order of $\sim$ 0.3 pW, a tolerable level of parasitic power dissipation in our setup would be about an order of magnitude lower, i.e., around 30 fW. This issue will be explored briefly in section 4.4.

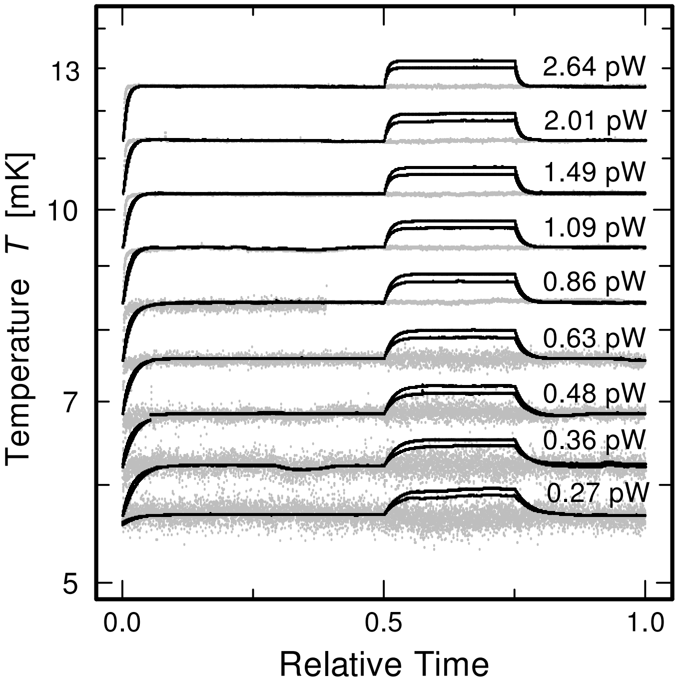

Fig. 4.2. Calculated values of the heat input onto sample #1, from the same measurement as the previous figure. The curves represent the mixing chamber temperature (gray), and the temperatures of the two Au:Er sensors.

The light absorber used on sample #1 was made of blackened aluminum tape of 80 μm thickness (3M Scotch tape 431), as this method can be easily applied to a hollow sample. However, we found that, above 22 mK, the presence of the Al absorber strongly disturbed the measurement. It appears that the upper sensor, which is only 1 mm away from the Al tape, could not reach thermalization even after a very long time. Figure 4.3 shows an example for this phenomenon. The exact cause of this effect has not been identified yet.

The thermal conductivity data we obtained for the sample made of F-320 (sample #2) are shown in Fig. 4.4. The temperature dependence of this data set can be described with an exponent $\beta = 1.90 \pm 0.10$, for $\kappa \propto T^{\beta}$. Here, no effects due to the absorber material were visible, hence the measurement could be performed over a larger temperature range. The absorber used on this sample was a black copper oxide (CuO) thin film (with a thickness of 700-800 nm), which was vapor-deposited onto the sample by the institute's cleanroom staff.

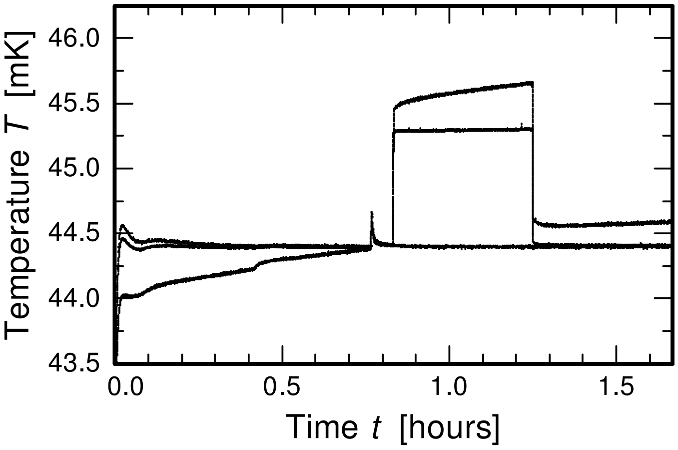

Fig. 4.3. Extract from a measurement on sample #1, with the temperatures of the mixing chamber (bottom curve) and the two paramagnetic sensors. At temperatures above 22 mK, the upper sensor is disturbed by the Al absorber, and has an extremely long thermalization time.

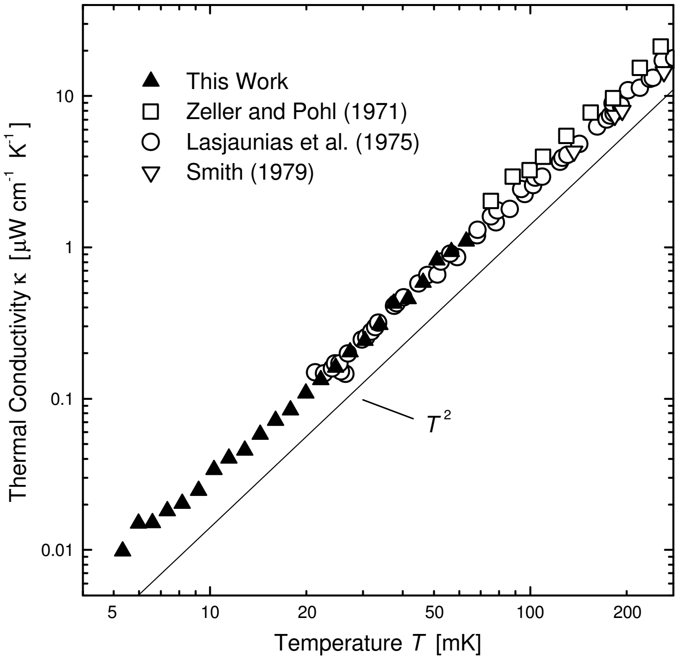

Fig. 4.4. Thermal conductivity κ of sample #2, made of the synthetic silica glass F-320. The T^2 curve has been added for comparison.

Our results for vitreous silica and for F-320 are consistent with the results of Lasjaunias, Ravex, Vandorpe, and Hunklinger (1975), who reported a temperature dependence of $T^{1.95}$ for the fused silica types Suprasil and Suprasil W, in the temperature range above 20 mK.

For BK7 glass (sample #3), we obtained the set of thermal conductivity data seen in Fig. 4.5. Fitting to a power law yields an exponent of $\beta = 2.10 \pm 0.10$. This is in contrast to the results of Rosenberg, Natelson, and Osheroff (2000), who reported finding an exponent of $\beta = 1.84$ for BK7 in the temperature range from 10 mK to 0.7 K.

The BK7 sample had an absorber made of black epoxy (STYCAST 2850) of a thickness of about 1 mm. Remarking that the epoxy had no ill effects on the performance of the measurement in the case of this sample, it is nonetheless advisable to avoid epoxy absorbers, as they tend to break the

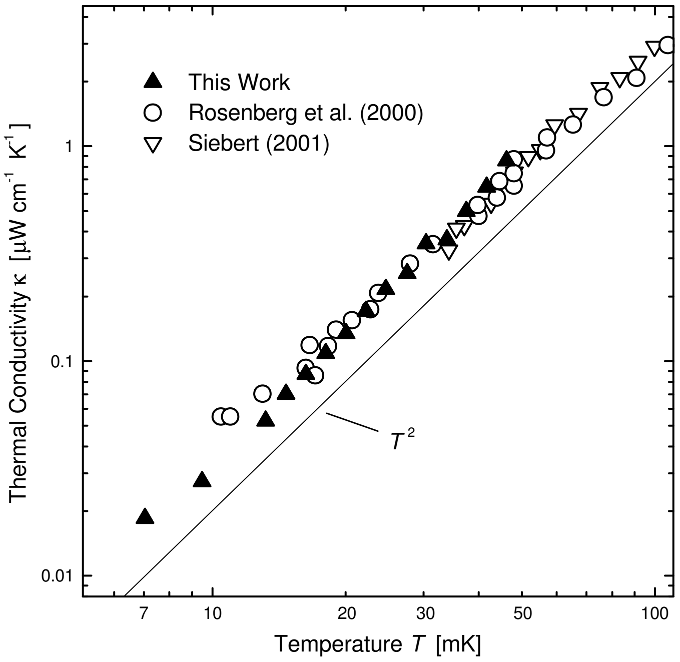

Fig. 4.5. Thermal conductivity κ of BK7 (sample #3). The T^2 curve is a guide to the eye.

glass sample during cool-down due to mechanical tension. Meanwhile, all massive samples to be used in our setup are furnished with CuO thin films. Besides, our findings with sample #1 suggest that, in order to avoid interference, the paramagnetic sensors should be positioned at a distance from the absorber.

The exponents β given above, which are obtained from fitting the thermal conductivity data from our measurements to a power law of the form $\kappa \propto T^{\beta}$, all have a rather large statistical error of ± 0.10. This is mainly due to the large scatter in the data points of the thermal conductivity κ at the lowest temperatures, around 5 to 7 mK. Our experiment is generally very sensitive to disturbances in the mixing chamber temperature. At higher temperatures, this does not pose a problem, since measurements can be performed rapidly, and the cryostat's temperature is very stable in this range. However, near the base temperature of the cryostat, the latter is easily disturbed by external influences, and the matter is worsened as the time needed for each temperature step of our measurement increases approximately as $1/T^2$ (see section 3.5.2). Major sources of disturbances to our experiment were ice-formation and the associated "ice cracking" in the liquid nitrogen dewar of our cryostat. Future measurements performed in a cryostat which has no nitrogen dewar are expected to yield results with less scatter even at lowest temperatures.

Our results at temperatures slightly higher than the cryostat's base temperature exhibit a significantly lower statistical error. When fitting our thermal conductivity data to a power law using the temperature range above 8 mK only, very similar values are found for the exponent β as the ones obtained for the full temperature range, but now with a reduced uncertainty of about ± 0.05.

4.2 Examination of the LED Heat Input

Since the heating method introduced in our experiment is new, it is necessary to verify that the results obtained with it are reliable. For this purpose, some test have been performed.

In Eq. (3.16), we have used the approximation that the thermal conductivity at a specific temperature, $\kappa(T)$, is proportional to the ratio between the heat input $\dot{Q}$ provided to the sample, and the temperature difference $\varDelta T$ arising between the two thermometers, i.e., $\kappa(T) \propto \dot{Q}/\varDelta T$. However, this will clearly not hold for an arbitrarily large heat input.

In the following, we will use the same notation as in section 3.5.2, denoting the relative temperature change occurring in the upper of the two sensors as $\varrho \equiv (T_1 - T_{\mathrm{MC}})/T_{\mathrm{MC}}$, where T_1 is the sensor's temperature in the steady state, and T_{MC} is the mixing chamber temperature.

In Fig. 4.6, data from a thermal conductivity measurement on sample #1 (vitreous silica) are shown, which was performed with constant heat input, i.e., the same repetition rate ν_{rep} of the voltage signal applied to the LED was used for all temperature steps. From the figure, it is apparent that the temperature change caused by the LED rapidly declines with rising temperature, from $\varrho \simeq 10\,\%$ around 10 mK, to $\varrho \simeq 1\,\%$ around 20 mK.

The thermal conductivity determined from this measurement is shown in Fig. 4.7. When fitting a power law of the form $\kappa \propto T^{\beta}$, the data are matched by an exponent $\beta = 1.97 \pm 0.12$. This value is similar to the exponent obtained above for the same sample, where a repetition rate that scaled

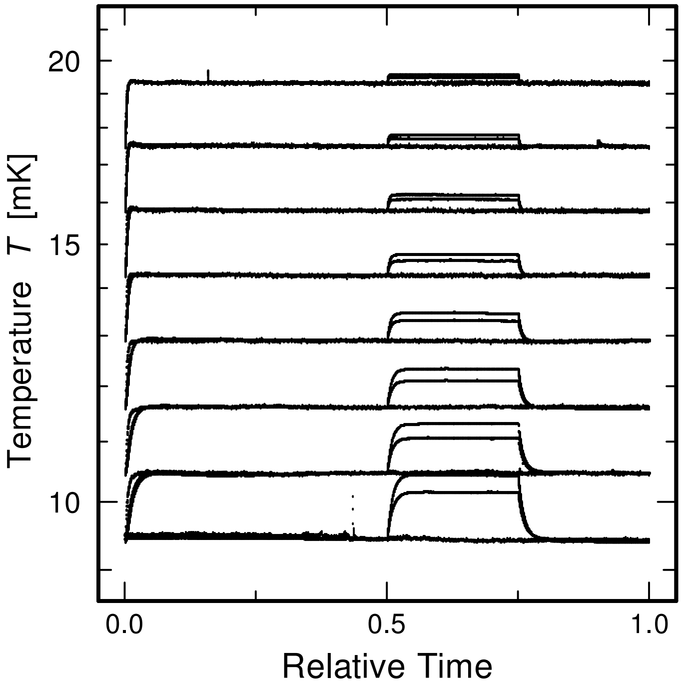

Fig. 4.6. Data from a thermal conductivity measurement, performed with temperature-independent heat input $\dot{Q}$. The curves represent the temperature of the cryostat's mixing chamber (bottom curve), and of the two paramagnetic sensors (top and middle curves). This measurement was performed on sample #1 (vitreous silica).

as $\nu_{\text{rep}} \propto T^3$ had been used. This indicates that, for $\varrho \lesssim 10\,\%$, our method will produce results for the thermal conductivity that do not depend on the amount of heat input.

Having established that the response of the sample to the heat input is linear, another test can be performed on the LED. In Eq. (3.17), it was assumed that the heat input onto the sample, $\dot{Q}$, is proportional to the LED signal's repetition rate ν_{rep}. However, this is not necessarily the case, e.g., at high repetition rates, the LED might heat up, which could change its characteristics.

Figure 4.8 shows data from a measurement, also performed on our vitreous silica sample #1, where the heat input applied to the sample was varied at fixed temperatures. At each temperature step T, we first used a repetition rate of the LED signal that scaled according to $\nu_{\text{rep}} \propto T^3$, as

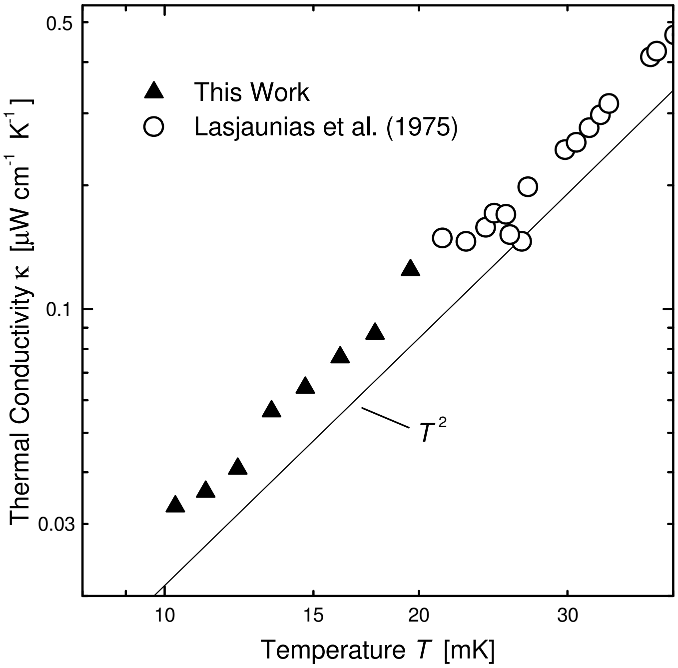

Fig. 4.7. Results for thermal conductivity κ, obtained from the measurement with constant heat input shown in Fig. 4.6.

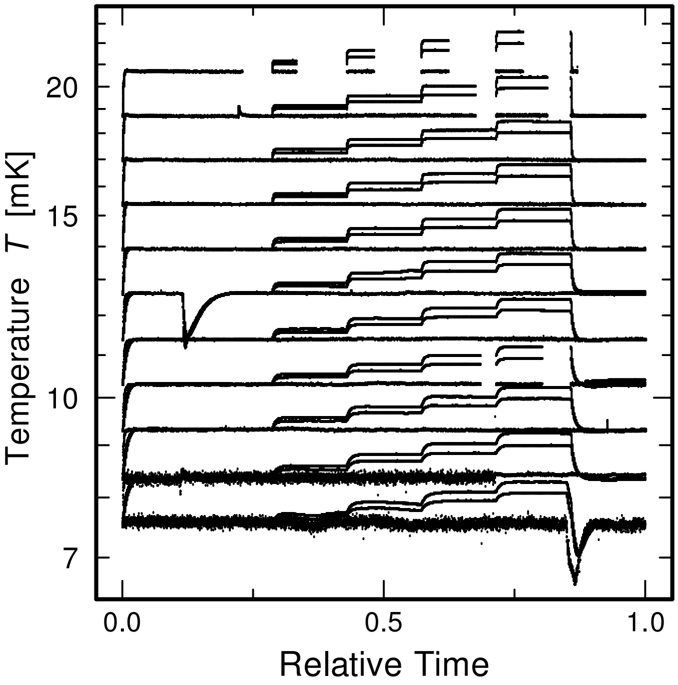

Fig. 4.8. Verifying the proportionality between heat input $\dot{Q}$ and the LED signal repetition rate ν_{rep}. The curves show the mixing chamber temperature (bottom curve), and the temperature of the two <u>Au</u>:Er sensors (top and middle curves). The measurement was performed on sample #1 (vitreous silica).
The gaps in the data set were introduced by the experimenters when “jumping” to the next measurement phase, usually in order to speed up the data acquisition when maintenance of the cryostat became necessary.

in previous measurements, and waited until the sample reached a steady state. This process was then repeated, with consecutive LED signal repetition rates of $2\,\nu_{\text{rep}}$, $3\,\nu_{\text{rep}}$, and $4\,\nu_{\text{rep}}$. In the upper one of the paramagnetic sensors, the four different amounts of heat input led to relative temperature changes of about $\varrho \simeq 2.5\,\%$, $5\,\%$, $7.5\,\%$, and $10\,\%$, respectively.

The resulting data sets of the thermal conductivity are shown in Fig. 4.9. All four data sets were fit to the literature values with one single parameter. As it appears from this measurement, the thermal conductivity determined with our method is not influenced by changing the repetition rate ν_{rep}. For all four different amounts of heat input, our results follow the same power law, with

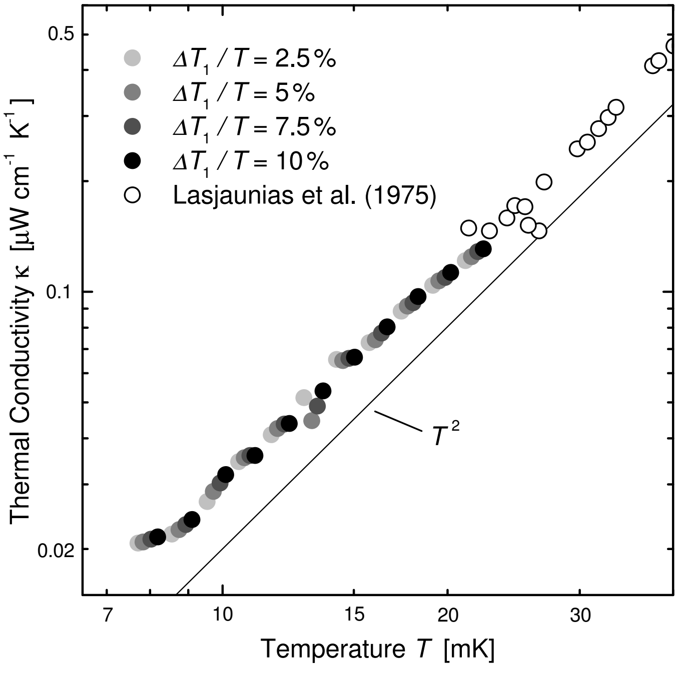

Fig. 4.9. Thermal conductivity κ, determined for four different levels of heat input. These results have been obtained from the data set shown in Fig. 4.8.

an exponent $\beta = 1.92 \pm 0.10$. This shows that, at least for $\varrho \lesssim 10\,\%$, the relative temperature change ϱ is proportional to ν_{rep}. Hence we verified that $\dot{Q} \propto \nu_{\mathrm{rep}}$.

4.3 Accuracy of the Thermometers

The level of statistical noise exhibited by the signals of our SQUID thermometers are a measure for the accuracy of this thermometry method. Figure 4.10 shows an interval of simultaneous temperature readings, of the paramagnetic susceptibility thermometer, which has been described in section 3.2.3, and of one of the SQUID thermometers measuring the magnetization of an Au:Er sensor attached to the glass sample.

Note that in this figure, we have calibrated the SQUID thermometer to the temperature reading of the paramagnetic susceptibility thermometer, rather than to the carbon resistance thermometer. Though this is contrary to our proceeding in all other sections of this thesis, it is done here for clarity; the statistical noise exhibited by the carbon thermometer would suggest great fluctuations in the mixing chamber temperature, though this temperature is in fact very stable.

From the figure, it is apparent that the noise level of our SQUID thermometers is extremely small, with a standard deviation around 0.8 µK, at a temperature of about 7.5 mK. Since this effect is smaller than the level of temperature fluctuations which occur in the cryostat, we will not need to consider it further as a possible source of errors.

However, though the relative accuracy of our SQUID thermometers is very high, the absolute temperature determined from them cannot be more accurate than the absolute temperature reading of the carbon resistance thermometer, due to our method of calibrating the SQUID thermometers. As noted in section 3.2.2, the temperature readings from the carbon thermometer

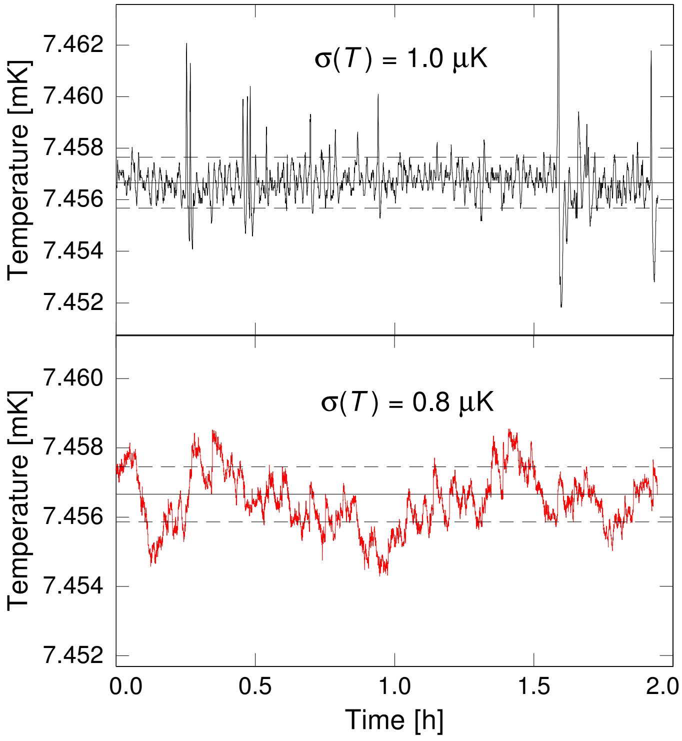

Fig. 4.10. Statistical noise in the signals of the paramagnetic susceptibility thermometer situated in our cryostat's mixing chamber (above), and of one of the paramagnetic SQUID thermometers (below).

have, at temperatures around 5 mK, an accuracy of about 5 %. Hence, the absolute temperature determined from the paramagnetic sensors attached to the sample is limited to this accuracy also.

4.4 Parasitic Heat Input

Due to the poor thermal conductivity of amorphous materials, and to their low heat capacity, our experimental setup cannot tolerate large amounts of parasitic power dissipation. Typical values of the intended heat input into the glass sample (see Fig. 4.2) suggest an upper limit for the tolerable parasitic heat input of about 20-30 femtowatts (fW) for measurements down to 5 mK.

In order to check whether the measurements presented here have been performed under circumstances in which the parasitic power dissipation does not exceed this limit, we have estimated the largest possible amount of parasitic heat input to our system.

In our experimental setup, any ac noise present in the pick-up coils will generate fluctuating magnetic fields, which in turn induce eddy currents in the Au:Er sensors. The heating due to these eddy currents can be expressed as (Pobell 1992)

$$\dot{Q}_{\text{eddy}} = \frac{G\,V}{\rho}\,|\dot{\boldsymbol{B}}|^2\,, \tag{4.2}$$

where $\boldsymbol{B}$ is the magnetic field strength, V and ρ are the volume and the resistivity of the sensor material, and G is a geometry factor. Hence, ac noise at higher frequency will cause stronger heating than noise at low frequencies.

To filter out noise in the frequency range above 100 kHz, we have installed a resistor ($r \simeq 10$ m) in parallel with the pick-up coil. This resistor itself is also a source of noise (Nyquist 1928). However, the noise spectrum of the resistor is mainly at low frequencies, and it turns out that it generates eddy current heating only of the order 10^{-18} W. Overall, the resistor r significantly reduces the noise level.

Next, we consider back-action from the SQUIDs. In a dc SQUID, a shunt resistor is placed across each Josephson junction ($R_{\mathrm{s}} \sim 2.5$), which in our setup also transmits its noise current, via the SQUID input coil, to the pick-up loop. The frequency of this type of noise can be as high as several gigahertz.

Furthermore, as the dc SQUID operates at a non-zero voltage, the current at the SQUID loop will oscillate at the Josephson frequency $f_{\mathrm{J}} = e\,U_{\mathrm{SQUID}}/\pi\hbar$, which is about 10 GHz. We estimate that this high-frequency noise can cause heating on the order of 10 fW. Therefore, assuming a maximum tolerable parasitic heat input of 20-30 fW at a temperature of 5 mK, we find that the SQUID back-action effects do not disturb our present measurements.

However, considering that the heating $\dot{Q}$ used to generate the temperature gradient within the glass sample is scaled as $\dot{Q} \propto T^3$, measurements slightly below 5 mK might already be disturbed by parasitic heat input due to the SQUID. Even though the estimate given here is only an upper limit for the heating caused by SQUID back-action, if any measurements are to be performed at temperatures around or below 1 mK, it will almost certainly be necessary to install appropriate filters.

4.5 Boundary Resistance

In the data evaluation procedure used in our experiment, it is assumed implicitly that the LED heating applied to the glass sample generates a temperature profile which is linear. We have used a finite element computer simulation to verify that this assumption is valid for our experimental setup.

Our simulation program has been developed using the software package ABAQUS.[1] For a given set of input data, it calculates the temperature distribution in our experimental setup. These input parameters are the geometry of the glass sample, the copper holder, and the Au:Er sensors, as well as their thermal transport properties. In the case of glass, we use the thermal conductivity data obtained in our experiment, whereas the properties of copper and Au:Er are found in the literature (Pobell 1992, Herrmannsdörfer, König, and Enss 2000).

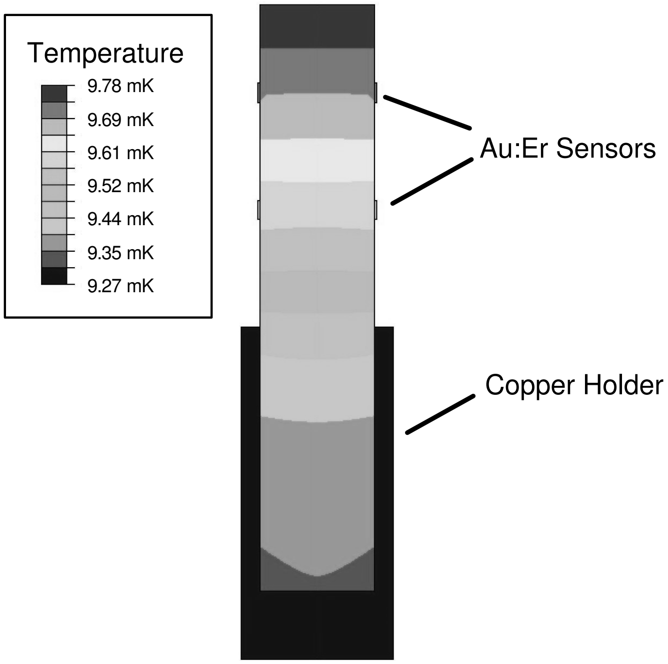

Fig. 4.11. Temperature profile of our experimental setup, calculated using a finite element computer simulation.

For each temperature step, boundary conditions for the simulation are given by the mixing chamber temperature T_{MC}, and the heat input $\dot{Q}$. A third boundary condition, the thermal resistance R_{K} (Kapitza resitance) at the glass/copper and glass/Au:Er interfaces, is not known. Hence, we perform the simulation as a parametric study, i.e., starting from an initial guess for R_{K}, we iterate the simulation with varying values of R_{K}. This is done until the resulting temperature distribution is in agreement with our measurement results, i.e., the values we determined experimentally for the paramagnetic sensors' temperature, T_1 and T_2, are reproduced by the simulation.

In Fig. 4.11, the temperature distribution in our glass sample, which has been obtained from our simulation program, is shown. The various grey shades indicate different temperatures. It can be seen that in the vicinity of the Au:Er sensors, the temperature profile is slightly distorted as the metallic sensors act as thermal shunts. However, we find that the temperature distribution between

---

[1] ABAQUS 6.3-4. Distributed by ABACOM Software GmbH, Aachen.

the two thermometers is linear to a very good approximation, hence the linearity assumption made in our evaluation procedure is valid.

As a byproduct, we obtain the thermal boundary resistance data shown in figures 4.12 and 4.13, for the boundaries Cu/STYCAST 1266/BK7, and Cu/STYCAST 1266/vitreous silica, respectively.

At temperatures above 50 mK, our data for R_{K} obtained from the measurements on BK7 are similar to the thermal boundary resistance found at typical Cu/varnish/dielectric interfaces (Ackerman and Anderson 1982), which usually exceeds the value predicted by acoustic mismatch theory (Little 1959) by more than an order of magnitude. (The surface of the dielectric has usually been damaged during cool-down, due to a large difference in thermal expansion between the materials, and the cracks at its surface prevent good thermal contact.)

However, our results for $R_{\mathrm{K}}T^3A$ do not exhibit the temperature-independent behavior found by Ackerman and Anderson (1982) for temperatures above 0.1 K; with decreasing temperature, our data approach the value predicted by acoustic mismatch theory. A possible interpretation for this is the following. With decreasing temperature, the wavelength of the dominant phonons increases, and above a certain wavelength, small defects at the interface no longer prevent the phonons from crossing the interface.

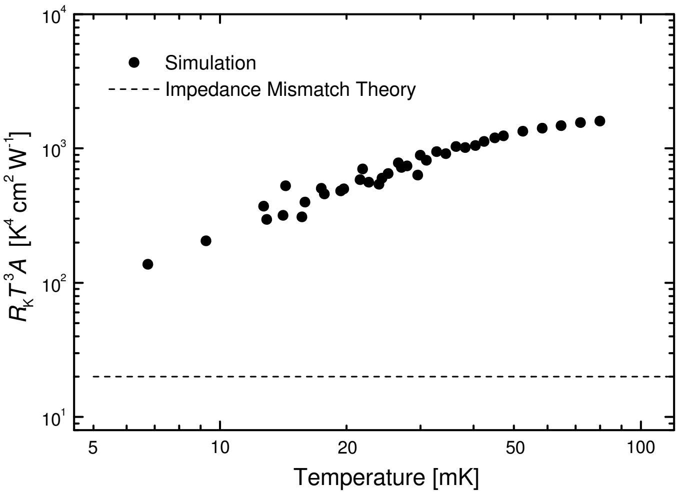

Fig. 4.12. Thermal boundary resistance at the interface Cu/STYCAST 1266/BK7, calculated with a finite element computer simulation. These data are based on combined results from several of our thermal conductivity measurements.

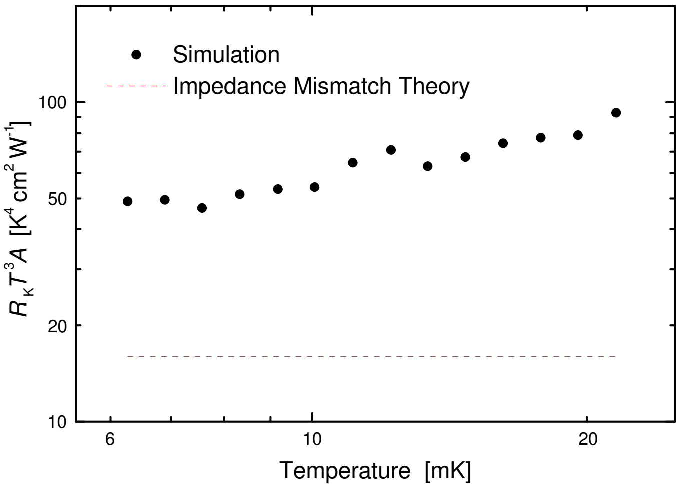

Fig. 4.13. Thermal boundary resistance at the interface Cu/STYCAST 1266/vitreous silica.

By extrapolation of our data shown in Fig. 4.12, it seems possible that the boundary resistance R_K will reach the theoretical limit at 2 mK. At this temperature, the wavelength of the dominant phonons is $\lambda_\mathrm{dom} \simeq 1$ µm, which indicates that the size of the defects at the boundary is probably in the micrometer range. By extending the temperature range of our measurements to lower temperatures, this issue could be investigated further.

5. Conclusion and Outlook

In this thesis, a technique has been presented which facilitates thermal conductivity measurements on dielectric materials in a previously inaccessible temperature range, i.e., below 10 mK. Our technique features an extremely low parasitic power dissipation into the sample, which is of the order of 10 fW. This has been accomplished by combining a contact-free SQUID thermometry technique, which makes use of the temperature-dependent magnetization of the paramagnetic substance Au:Er, with a method to heat the sample optically. In this manner, electrical contacts to the glass sample are altogether avoided.

We have presented thermal conductivity measurements performed on samples of the glass types BK7, vitreous silica, and F-320, which reach down to temperatures of about 7 mK, 6 mK, and 5 mK, respectively. For these samples, we have found a temperature dependence of the form of a power law, i.e. $\kappa \propto T^{\beta}$, with $\beta = 2.10 \pm 0.10$ in the case of BK7, and $\beta = 1.90 \pm 0.10$, for vitreous silica and F-320. In the latter case, our findings are in agreement with the value $\beta = 1.95$ found by Lasjaunias, Ravex, Vandorpe, and Hunklinger (1975), whereas in the case of BK7, our result contradicts a report of a much smaller temperature dependence ($\beta = 1.84$) of the thermal conductivity found in this material by Rosenberg, Natelson, and Osheroff (2000). All of our results do not significantly differ from the Standard Tunneling Model's prediction of a quadratically temperature-dependent thermal conductivity.

From the thermal conductivity data of our glass samples, using a finite element computer simulation, we have calculated an approximate temperature dependence of the thermal boundary resistance, for the cases of the boundaries copper/STYCAST 1266/vitreous silica, and copper/STYCAST 1266/BK7. Our results for R_{K} deviate from the temperature dependence reported for metal/epoxy/dielectric contacts at temperatures above 0.1 K, which is governed by small cracks in the dielectric's surface (Ackerman and Anderson 1982), and instead decrease towards the value predicted by acoustic mismatch theory. We attribute this effect to the dominant phonon wavelength approaching the typical dimension of the surface defects with decreasing temperature.

For future studies of the thermal conductivity of amorphous materials, investigating the predictions of the Standard Tunneling Model and possible deviations thereof, two approaches may be employed. One of these is to extend the operating range of our technique to temperatures below 5 mK, which can be reached in a nuclear demagnetization cryostat. For this, however, a number of difficulties have to be overcome. The most prominent of these are the SQUID back-action effects described in the previous section, causing a parasitic heat input for which we have estimated an upper limit of 10 fW. Such heat input can be prevented only by installing appropriate filters. Another impediment are the long relaxation time and the time-dependent heat release occurring in amorphous materials at low temperatures, requiring the use of samples of very small dimensions, and thus also of minute paramagnetic Au:Er sensors, where for the latter the strong rise in heat capacity towards lower temperatures poses yet another challenge. Moreover, the sensor substance Au:Er reaches a spin-glass state at low temperatures, prohibiting its use as a thermometer. This transition can be delayed to lower temperatures by lowering the erbium concentration; however, as a consequence, the signal amplitude will be reduced.

The other approach, which can be realized in the short-term, is to subject other types of glass samples to our present measurement technique, in order to improve the statistics on available thermal conductivity data down to about 5 mK. Interesting candidates for this would be, e.g., multi-component glasses such as barium aluminosilicate glass, or glasses with high lead content, which are more likely to exhibit deviations from the Standard Tunneling Model due to the strong interactions between the tunneling systems. Also, several technical improvements can be realized on our present setup. First, a considerable improvement of the thermal contact between the glass sample and its copper holder can be expected through the use of an intermediate copper foil, resulting in a reduced relaxation time of the system. Another possible enhancement concerns the pick-up coils which, rather than being cast in STYCAST 1266, could be wrapped onto a hollow gold cylinder. This would both improve the shielding of the paramagnetic sensors against high-frequency radiation originating from the SQUIDs, and introduce an additional noise contribution to the picked-up signal. While, due to our averaging procedure, the noise would not disturb the performance of our measurement, this arrangement would constitute a noise thermometer that could be used for a more accurate temperature calibration of our paramagnetic sensors.

Summarizing, we believe that the presented measurement technique has ample potential in the future investigation of the low temperature thermal transport properties of amorphous materials.

Ackerman, D. A., and A. C. Anderson (1982): *Rev, Sci. Instrum.* **53**, 100.

Anderson, P. W., B. I. Halperin, and C. M. Varma (1972): *Philos. Mag.* **25**, 1.

Arnold, W., and S. Hunklinger (1975): *Solid State Commun.* **17**, 883.

Black, J. L. (1978): *Phys. Rev. B* **17**, 2740.

Black, J. L., and B. I. Halperin (1977): *Phys. Rev. B* **16**, 2879.

Burin, A. L. (1995): *J. Low Temp. Phys.* **100**, 309.

Burin, A. L., L. A. Maksimov, and I. Y. Polishchuk (1989): *JETP Lett.* **49**, 784.

Clarke, J. (1996): in *SQUID Sensors: Fundamentals, Fabrication and Applications*. Kluwer Academic Publishers, Netherlands.

Clarke, J., W. M. Goubau, and M. B. Ketchen (1976): *J. Low Temp. Phys.* **25**, 99.

Classen, J., T. Burkert, C. Enss, and S. Hunklinger (2000): *Phys. Rev. Lett.* **84**, 2176.

Enss, C., A. Fleischmann, K. Horst, J. Schönefeld, J. Sollner, J. S. Adams, Y. H. Huang, Y. H. Kim, and G. M. Seidel (2000): *J. Low Temp. Phys.* **121**, 137.

Enss, C., and S. Hunklinger (2000): *Tieftemperaturphysik*. Springer-Verlag, Heidelberg.

Eska, G., and K. Neumaier (1983): *Cryogenics* February 1983, 84.

Fleischmann, A. (1998): Diploma Thesis, Univ. Heidelberg.

Fleischmann, A., J. Schönefeld, J. Sollner, C. Enss, J. S. Adams, S. R. Bandler, Y. H. Kim, and G. M. Seidel (2000): *J. Low Temp. Phys.* **118**, 7.

Freeman, J. J., and A. C. Anderson (1986): *Phys. Rev. B* **34**, 5684.

Herrmannsdörfer, T., and R. König (2000): *J. Low Temp. Phys.* **118**, 45.

Herrmannsdörfer, T., R. König, and C. Enss (2000): *Physica B* **284-288**, 1698.

Heuer, A. (1998): in *Tunneling Systems in Amorphous and Crystalline Solids*. Springer-Verlag, Berlin, Heidelberg.

Horst, K. (1999): Diploma Thesis, Univ. Heidelberg.

Hunklinger, S. (2001): *Festkörperphysik*. Lecture Notes.

Hunklinger, S., and W. Arnold (1976): in *Physical Acoustics, Vol. XII*. Academic Press, New York.

Hunklinger, S., and A. K. Raychaudhuri (1986): in *Progress in Low Temperature Physics, Vol. IX*. Elsevier, Amsterdam.

Jäckle, J. (1972): *Z. Physik* **257**, 212.

Jäckle, J., L. Piché, W. Arnold, and S. Hunklinger (1976): *J. Non-Cryst. Solids* **20**, 365.

Kagan, Y., L. A. Maksimov, and I. Y. Polishchuk (2000): *JETP Lett.* **71**, 69.

Kapitza, P. L. (1941): *J. Phys. USSR* **4**, 181.

Kittel, C. (1963): *Quantum Theory of Solids*. Wiley, New York.

——— (1996): *Introduction to Solid State Physics*. Wiley, New York.

Lasjaunias, J. C., A. Ravex, M. Vandorpe, and S. Hunklinger (1975): *Solid State Commun.* **17**, 1045.

Little, W. A. (1959): *Can. J. Phys.* **37**, 334.

London, H., G. R. Clarke, and E. Mendoza (1962): *Phys. Rev.* **128**, 1992.

Nyquist, H. (1928): *Phys. Rev.* **32**, 110.

Phillips, W. A. (1972): *J. Low Temp. Phys.* **7**, 351.

——— (1981): in *Topics in Current Physics, Vol. 24*. Springer-Verlag, Berlin, Heidelberg.

Piché, L., R. Maynard, S. Hunklinger, and J. Jäckle (1974): *Phys. Rev. Lett.* **32**, 1426.

Pobell, F. (1992): *Matter and Methods at Low Temperature*. Springer, Heidelberg.

Pohl, R. O., W. F. Love, and R. B. Stephens (1974): in *Proceedings of the 5th International Conference on Amorphous and Liquid Semiconductors, Vol. II*. Taylor & Francis, London, 1121.

Rogge, S., D. Natelson, and D. D. Osheroff (1996): *Phys. Rev. Lett.* **73**, 268.

Rosenberg, D., D. Natelson, and D. D. Osheroff (2000): *J. Low Temp. Phys.* **120**, 259.

Salvino, D. J., S. Rogge, B. Tigner, and D. D. Osheroff (1994): *Phys. Rev. Lett.* **73**, 268.

Siebert, L. (2001): Ph.D. Thesis, Univ. Heidelberg.

Smith, T. L. (1979): Ph.D. Thesis, Univ. of Illinois.

Stephens, R. B. (1973): *Phys. Rev. B* **8**, 2896.

Strehlow, P., C. Enss, and S. Hunklinger (1998): *Phys. Rev. Lett.* **80**, 5361.

Strehlow, P., and M. Meissner (1999): *Physica B* **263-264**, 273.

Strehlow, P., M. Wohlfahrt, A. G. M. Jansen, R. Haueisen, G. Weiss, C. Enss, and S. Hunklinger (2000): *Phys. Rev. Lett.* **84**, 1938.

Swartz, E. T., and R. O. Pohl (1989): *Rev. Mod. Phys.* **61**, 605.

Tao, L. J., D. Davidov, R. Orbach, and E. P. Chock (1971): *Phys. Rev. B* **4**, 5.

Weis, R. (1995): Ph.D. Thesis, Univ. Heidelberg.

Williams, G., and L. L. Hirst (1969): *Phys. Rev.* **185**, 407.

Würger, A., and D. Bodea (2003): private communication.

Zaitlin, M. P., and A. C. Anderson (1975): *Phys. Rev. B* **12**, 4475.

Zeller, R. C., and R. O. Pohl (1971): *Phys. Rev. B* **4**, 2029.

Acknowledgements

I would like to sincerely thank all these who have supported me in any way while I pursued my Diploma project. Particularly I would like to express my gratitude to

- my advisor Dr. Christian Enss, for offering me the opportunity and the means to perform this exciting project in his research group. I am grateful for the discussions we had about the course of the experiment, and I thank him for the support and advice he has provided.
- Prof. S. Hunklinger, for his lively interest in our experiment, as well as for offering to be the co-assessor of this thesis. I would like to mention that it was his excellent course on condensed matter physics that initially brought me to this research group.
- my colleague Dr. Hsin-Yi Hao, for providing kind and constant guidance to me all during this year. Most of our project's success is due to her intuition, experience, and incessant effort. Besides, I thank her for thoroughly proof-reading this thesis.
- our team leader Andreas Fleischmann, for introducing me to the "κ project", and for very patiently teaching me the basics of low temperature physics. His competence and skill have helped to solve a great many problems in this project.
- all my collegues in the research group, who have made working here so enjoyable and unique: Dr. Markus Heitz, Marc Layer, Astrid Netsch and Xuewei Cao from the "Noble Gas Lab", Talgat Daniyarov, Markus Linck, Hannes Rotzinger, and Andreas Burck from the "Bolometer Lab", Dr. Gernot Kasper and Andreas Reiser from the "High Pressure Lab", and Dr. Peter Nagel and Maximilian Brandt from the "Big Lab".
- Dr. Robert Weis, for his assistance in all matters related to computers, and Dr. Jens Wagner, for his help in designing electronic circuits.
- all the members of the Kirchhoff Institute who provided the technical assistance for our project. Especially I would like to mention the outstanding efforts of Mr. S. Spiegel (student workshop), Mr. T. Wolf and Mr. V. Schultheiss (cleanroom), Mr. P. Frauenfeld and Mr. R. Weidner (electronics workshop), and Mr. R. Gradt (cryoliquids).
- Mr. R. Stadler and Mr. W. Kretschmar from the glass workshop at the Physical Institute, for the very careful preparation of the glass samples.
- Dr. P. Strehlow (PTB Berlin), for providing us with the BK7 and F-320 samples, and Mr. R. Twickler (ABACOM Software GmbH, Aachen) who put a license of the finite element software ABAQUS at our disposal.

Finally I would like to thank my parents and my family, only through whom my studies have become possible, and all my friends, for being so sympathetic and patient with me over the past few months.

Erklärung:

Ich versichere, daß ich diese Arbeit selbständig verfaßt und keine anderen als die angegebenen Quellen und Hilfsmittel benutzt habe.

Heidelberg, den ________________ ______________________________

Unterschrift